

RESEARCH ARTICLE

Open Access



A new mechanical perspective on a shallow megathrust near-trench slip from the high-resolution fault model of the 2011 Tohoku-Oki earthquake

Tatsuya Kubota^{1*} , Tatsuhiko Saito¹  and Ryota Hino² 

Abstract

The 2011 Tohoku-Oki earthquake generated a surprisingly large near-trench slip, and earth scientists have devoted significant attention to understanding why. Some studies proposed special rupture mechanisms, such as extensive dynamic frictional weakening; others simulated this near-trench slip behavior without supposing the extensive dynamic weakening. However, we have not reached a decisive conclusion for this question due to limited spatial near-trench slip resolution. Hence, in this study we use new tsunami data recorded just above the large slip area in addition to offshore and onshore geodetic data to improve the spatial resolution of stress release in the Tohoku-Oki earthquake and quantitatively examine the mechanical state of the plate interface. A maximum slip of 53 m reaching the trench and an insignificant stress drop (< 3 MPa) at the shallowest portion of the fault were estimated. Based on our modeling results and the past experimental studies, it is suggested that friction at the shallow near-trench portion should be inherently low both before and during the earthquake. This result provides perspectives on the shallow slip behavior along the plate boundary, in which the strain energy accumulation at the deep portion of the fault accounts for the anomalous large shallow slip, but shallow mechanical coupling does not. A large shallow slip has been considered as a result of the release of sufficiently large strain energy at the shallow portion of the plate interface, but we suggest that shallow slips similar to that during the 2011 Tohoku-Oki earthquake may occur in any subduction zones where the energy sufficiently accumulates only in the deeper portion.

Keywords: The 2011 Tohoku-Oki earthquake, Ocean-bottom pressure gauge, Tsunami, Stress drop, Frictional strength of megathrust, Plate mechanical coupling

1 Introduction

The devastating tsunami generated by the 2011 Tohoku-Oki earthquake caused severe damage to the coast of Japan. The most surprising feature of this megathrust earthquake is the occurrence of a very large slip (> 50 m) reaching the trench (Kodaira et al. 2012; 2020; Sun et al. 2017). Before this earthquake, it was widely

believed that the interface between the two plates at the shallow portion, corresponding to a depth range shallower than ~ 10 km from the seafloor, was stably sliding (creeping) during the interseismic period, resulting in no stress accumulation (i.e., no mechanical coupling) (Byrne et al. 1988; Scholtz 1998; Bilek and Lay 2002). Only the deep portion of the plate interface (deeper than ~ 10 km) was believed to be locked to accumulate the stress (i.e., mechanically coupled), which exhibited unstable stick-slip (i.e., earthquake) behavior (Byrne et al. 1988; Scholtz 1998; Bilek and Lay 2002). The stable sliding behavior at the shallow portion was also considered to be consistent

*Correspondence: kubotatsu@bosai.go.jp

¹ National Research Institute for Earth Science and Disaster Resilience, 3-1 Tennodai, Tsukuba, Ibaraki 305-0006, Japan
Full list of author information is available at the end of the article

with almost no interseismic slip deficit near the trench estimated before the Tohoku-Oki earthquake (Suwa et al. 2006; Hashimoto et al. 2009; Loveless and Meade 2010; 2011) that was unlikely to have caused the large coseismic slip. To better understand shallow slip behavior and tsunami generation in subduction zones, it is crucial to clarify the reason for this unexpected extremely large slip occurring during the Tohoku-Oki earthquake. This study attempts to address this scientific issue, particularly focusing on the perspective of fault mechanics (i.e., stress accumulation and release), whereas many previous studies have discussed from the kinematic perspective (i.e., slip deficit and coseismic slip). Although the kinematic and mechanical perspectives are closely related to each other, we should note that these two concepts are essentially different but are often confusingly used to discuss the interseismic process (Wang and Dixon 2004).

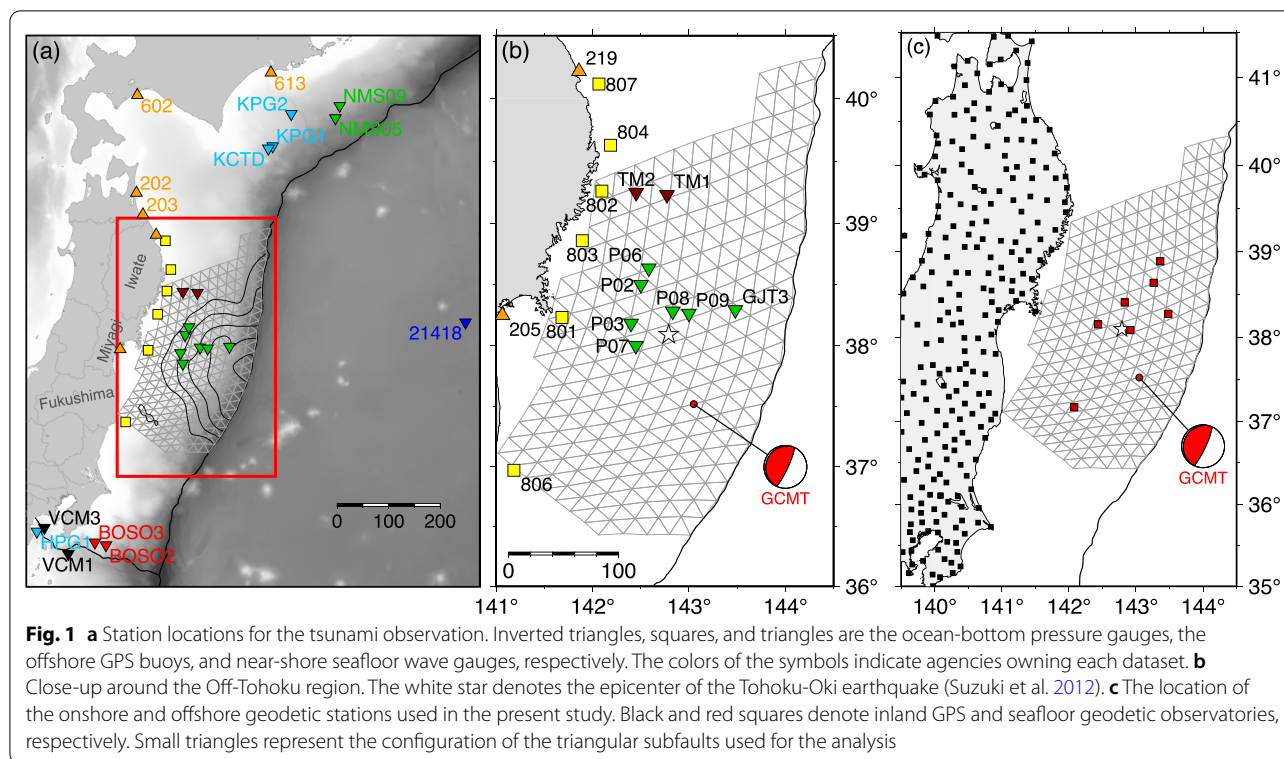
To explain this shallow slip behavior, some studies have considered that the frictional strength along the shallow plate interface is high enough to accumulate shear stress during the interseismic period. It has been proposed that when the Tohoku-Oki earthquake occurred, the shallow frictional stress extensively reduced with an increase in the slip rate (dynamic weakening) (Di Toro et al. 2011; Noda and Lapusta 2013), leading to a large shallow slip. An example of the dynamic frictional weakening mechanism related to frictional heating along the plate interface, called “thermal pressurization,” has also been proposed to explain the shallow slip behavior (Hirono et al. 2019; Shibazaki et al. 2019). The extensive reduction in frictional strength basically requires significant shear stress reduction at the shallow portion of the plate interface.

Other studies have attempted to explain the shallow slip behavior without considering these special mechanisms requiring a shallow large stress drop (e.g., Lay et al. 2012). The basic standpoint of the plate coupling and rupture mechanics in these studies is that the shallow portion of the plate boundary does not accumulate the shear stress but only the deep portion does, as has been conventionally thought (Sholtz 1998; Bilek and Lay 2002). From the observational facts, a seafloor drilling survey (Chester et al. 2013) showed the existence of a low-friction material along the Tohoku shallow fault zone (Fulton et al. 2013; Ujiie et al. 2013). A laboratory experiment of this shallow fault-zone material retrieved from the Tohoku subduction zone, under a water-dampened condition mimicking a plate boundary suggested that the low-friction material was insensitive to the slip rate (i.e., no extreme dynamic weakening behavior) (Remitti et al. 2015). Fukuyama and Hok (2015) conducted the dynamic earthquake rupture simulation of an interplate earthquake mimicking the Tohoku-Oki earthquake,

who assumed a large stress release region only at the deep portion of the plate interface corresponding to a strong mechanical plate locking (i.e., no stress release at the shallow portion). This dynamic rupture simulation showed the surface-reaching slip can occur without stress drop at the shallow portion, due to the stress-free boundary condition at the ground surface. In addition, based on fault mechanics, some recent modeling studies have pointed out that, a large shallow slip can occur because of the “pinning” effect of the deep frictionally locked area which causes slip delay (or slip deficit) in the shallow portion (Almeida et al. 2018; Herman and Govers 2020; Herman et al. 2018; Lindsey et al. 2021).

It is difficult to identify the shallow stress release process in detail because of the large uncertainty in the near-trench slip, owing to the lack of a dataset with sufficient quality to resolve it. Although seafloor geodetic data (Fujiwara et al. 2011; Kido et al. 2011; Sato et al. 2011) have made significant contributions toward elucidating the slip distribution (Iinuma et al. 2012; Sun et al. 2017), the spatial resolution of the slip inferred from such data, which contains information that is only relevant at the location of the observation point, is limited. The onshore seismic and geodetic datasets recorded more than 200 km from the trench axis also have difficulty in resolving the near-trench slip (e.g., Loveless and Meade 2015). The analyses using the seismograms also require the assumption of the rupture propagation velocity across the fault, but this assumption may cause an uncertainty in estimating the spatial extent of the entire slip region because of a substantial trade-off between the rupture velocity and the spatial extent (Kubota et al. 2018). The distributions of the coseismic slip and stress release proposed in the past vary from model to model, particularly at the shallowest portion (Brown et al. 2015; Sun et al. 2017; Lay 2018), due to the issues raised above. Therefore, the cause of the large shallow slip has been investigated for the past ten years, but no decisive conclusion has been reached.

In this study, we attempt to constrain the slip and stress drop distributions with the highest precision to reveal the cause of the near-trench large slip during the 2011 Tohoku-Oki earthquake and to understand the mechanics of the shallow trench-reaching rupture. To achieve this, we use the tsunami data recorded by several ocean-bottom pressure gauges installed directly above the fault area (Kubota et al. 2021), which have not before been utilized in a slip inversion for the event (Fig. 1). The tsunami data are advantageous to overcome this issue because shallow near-trench slips excite tsunamis more efficiently than the deeper slip and hence the tsunami waveform data contain unique and robust spatial information about



the distribution of the fault slip, in particular at the shallow portion near the trench.

2 Data and methods

2.1 Data

We use the tsunami data from ocean-bottom pressure gauges installed just above the large slip area (near-field data), obtained by Tohoku University (Kubota et al. 2021) (green inverted triangles in Fig. 1a and b). We also use the ocean-bottom pressure gauge data of the University of Tokyo (Maeda et al. 2011) off Iwate (dark red inverted triangles in Fig. 1b). The station information is summarized in Table 1.

We also use the offshore tsunami data obtained far from the source area (far-field data) from the ocean-bottom pressure gauges of the Japan Agency for Marine-Earth Science and Technology (JAMSTEC, light blue inverted triangles in Fig. 1a), Japan Meteorological Agency (JMA, red inverted triangles), National Research Institute for Earth Science and Disaster Resilience (NIED, black inverted triangles), and National Oceanic and Atmospheric Administration (NOAA)'s DART (Deep-ocean Assessment and Reporting of Tsunamis) system (a blue inverted triangle). We also use the tsunami waveforms from the GPS buoys (yellow squares in Fig. 1a and b) and the wave gauges (orange triangles) of NOWPHAS (Nationwide Ocean Wave information network for Ports

and HarbourS) of the Port and Airport Research Institute (PARI).

In the data processing of the tsunami data, we remove the tidal fluctuation using the theoretical model NAO.99Jb (Matsumoto et al. 2000). We then apply a low-pass filter with a cutoff period of 100 s to the near-field ocean-bottom pressure records and a band-pass filter with a passband of 100–3600 s to the other far-field tsunami data.

In addition to these tsunami dataset, we also use offshore geodetic observation data (Kido et al. 2011; Sato et al. 2011) and onshore GPS data obtained by the Geospatial Information Authority of Japan (GSI) (Fig. 1c).

2.2 Methods

2.2.1 Fault geometry and crustal deformation calculation

In contrast to most of the past tsunami modeling studies using the simplified fault configuration (e.g., Satake et al. 2013; Yamazaki et al. 2018), such as implementing a planar fault geometry, large-sized and discontinuous subfaults, and/or a buried fault with a top that does not reach the seafloor, we incorporate the nonplanar fault geometry of the Japan Integrated Velocity Structure Model (JIVSM) (Koketsu et al. 2012) for the analysis (Fig. 2a). This is because we intend to obtain the correct slip and stress drop distribution by suppressing spurious slip and stress drop and artificial stress

Table 1 List of tsunami stations used in this study

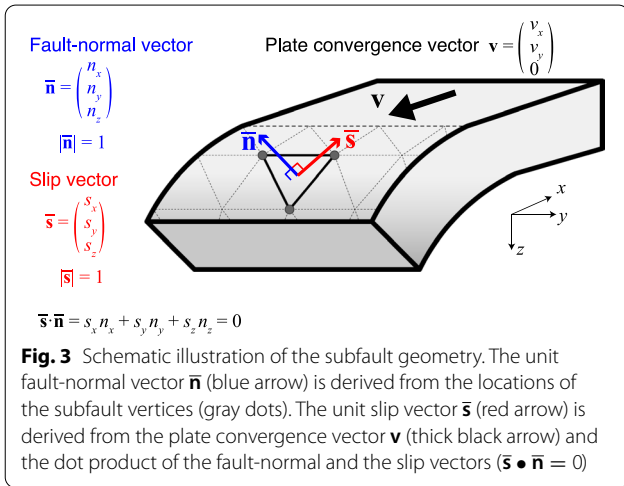
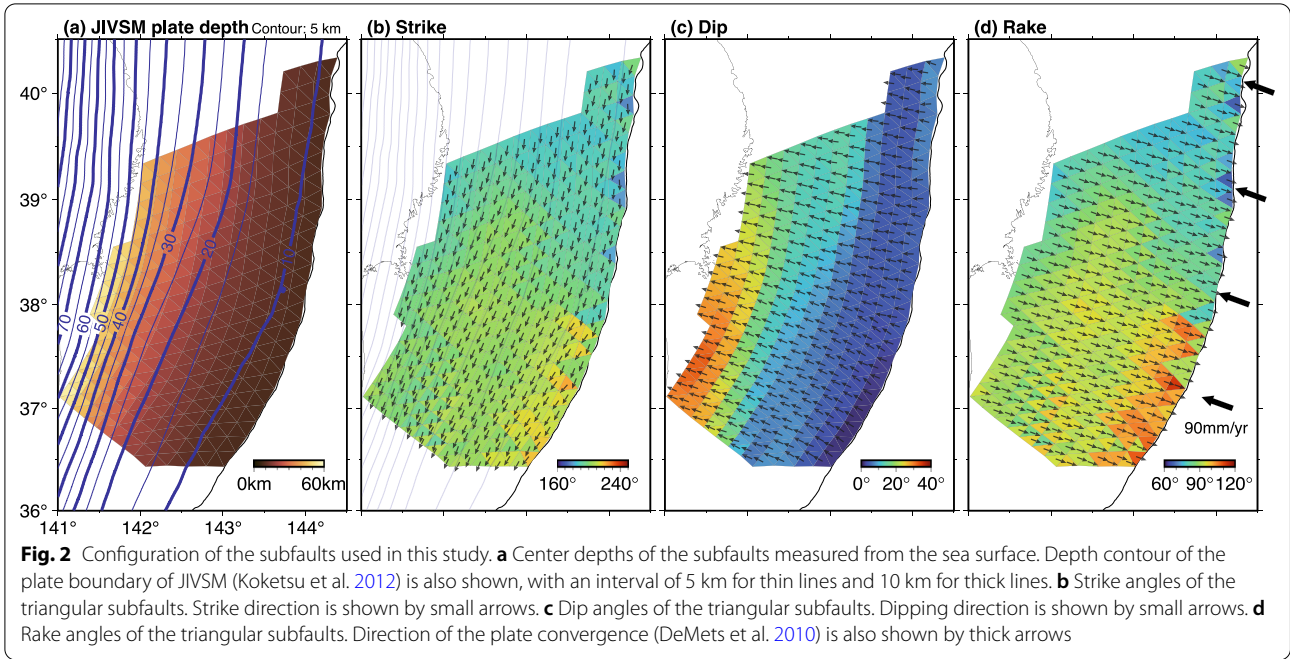
Station	Latitude [°N]	Longitude [°E]	Depth [m]	Inversion time window [s]	Agency	Sampling rate of original data [s] ^a
TM2	39.2459	142.4526	997	0–1800	ERI	0.1
TM1	39.2283	142.7720	1618	0–1800	ERI	0.1
P06	38.6340	142.5838	1254	0–3600	Tohoku University	1
P02	38.5002	142.5016	1104	0–3600	Tohoku University	1
P03	38.1834	142.3998	1052	0–3600	Tohoku University	1
P07	38.0016	142.4495	1059	0–3600	Tohoku University	1
P08	38.2829	142.8320	1418	0–3600	Tohoku University	1
P09	38.2650	143.0002	1556	0–3600	Tohoku University	1
GJT3	38.2945	143.4814	3293	0–3600	Tohoku University	1
21,418	38.7180	148.6980	5500	1200–4200	NOAA	15
KPG2	42.2365	144.8454	2210	600–3600	JAMSTEC	0.1
KPG1	41.7040	144.4375	2218	600–3600	JAMSTEC	0.1
KCTD	41.6675	144.3409	2540	600–3600	JAMSTEC	10
NMS09	42.3692	145.9167	3316	600–3600	Tohoku University	1
NMS05	42.1667	145.8235	4548	600–3600	Tohoku University	1
BOSO2	34.7550	140.7517	2098	600–4200	JMA	1
BOSO3	34.8050	140.5067	1912	600–4200	JMA	1
HPG1	35.0031	139.2247	1176	1800–5400	JAMSTEC	1
VCM3	35.0712	139.3906	1225	1800–5400	NIED	0.1
VCM1	34.5954	139.9198	2125	1800–5400	NIED	0.1
807	40.1167	142.0667	125	0–3600	NOWPHAS	5
804	39.6272	142.1867	200	0–3600	NOWPHAS	5
802	39.2586	142.0969	204	0–3600	NOWPHAS	5
803	38.8578	141.8944	160	0–3600	NOWPHAS	5
801	38.2325	141.6836	144	0–3600	NOWPHAS	5
806	36.9714	141.1856	137	0–3600	NOWPHAS	5
613	42.9106	144.3972	50.0	1800–5400	NOWPHAS	5
602	42.5439	141.4458	50.7	1800–5400	NOWPHAS	5
202	40.9250	141.4242	43.8	1800–4800	NOWPHAS	5
203	40.5608	141.5683	27.7	Not Used	NOWPHAS	5
219	40.2178	141.8600	49.5	Not Used	NOWPHAS	5
205	38.2500	141.0661	21.3	Not Used	NOWPHAS	5

^a All observed records were resampled to 1 s in the inversion analyses

discontinuity around the boundaries of the subfaults (e.g., Hu and Wang 2008; Ma 2012; Brown et al. 2015; Wang et al. 2018; Du et al. 2021). The detail is described in Texts S1 and S2 in Additional file 1.

To derive the fault slip distribution through Green's functions, the nonplanar fault plane is divided into small triangular subfault elements, in which the length of one side of the triangle is approximately 10 km (triangles in Figs. 1 and 2). In this fault triangulation, the longitude and latitude of the subfault vertices are identical to those of Inuma et al. (2016) but our triangulation used the plate depths from JIVSM (Koketsu et al. 2012), while those of Nakajima and Hasegawa (2006) were used in Inuma et al. (2016). The total number of

the triangular subfaults used in this study is $N_{\text{sub}} = 434$. Using these triangular subfault elements, we calculate the seafloor displacement using a uniform half-space structure model (Meade 2007). To correctly simulate the trench-reaching rupture (Wang et al. 2018) in the half-space, we slightly modify the fault configuration as follows. First, the depths of all the triangular vertices are systematically moved vertically upward by 8 km to discard the seawater layer. Then, the depths of the uppermost row of triangular subfaults (i.e., the computational free surface) are set to 0 km from the free surface so that the shallowest fault surface lines up with the trench axis. We show the strike and dip angles derived from the JIVSM in Fig. 2b and c, which are



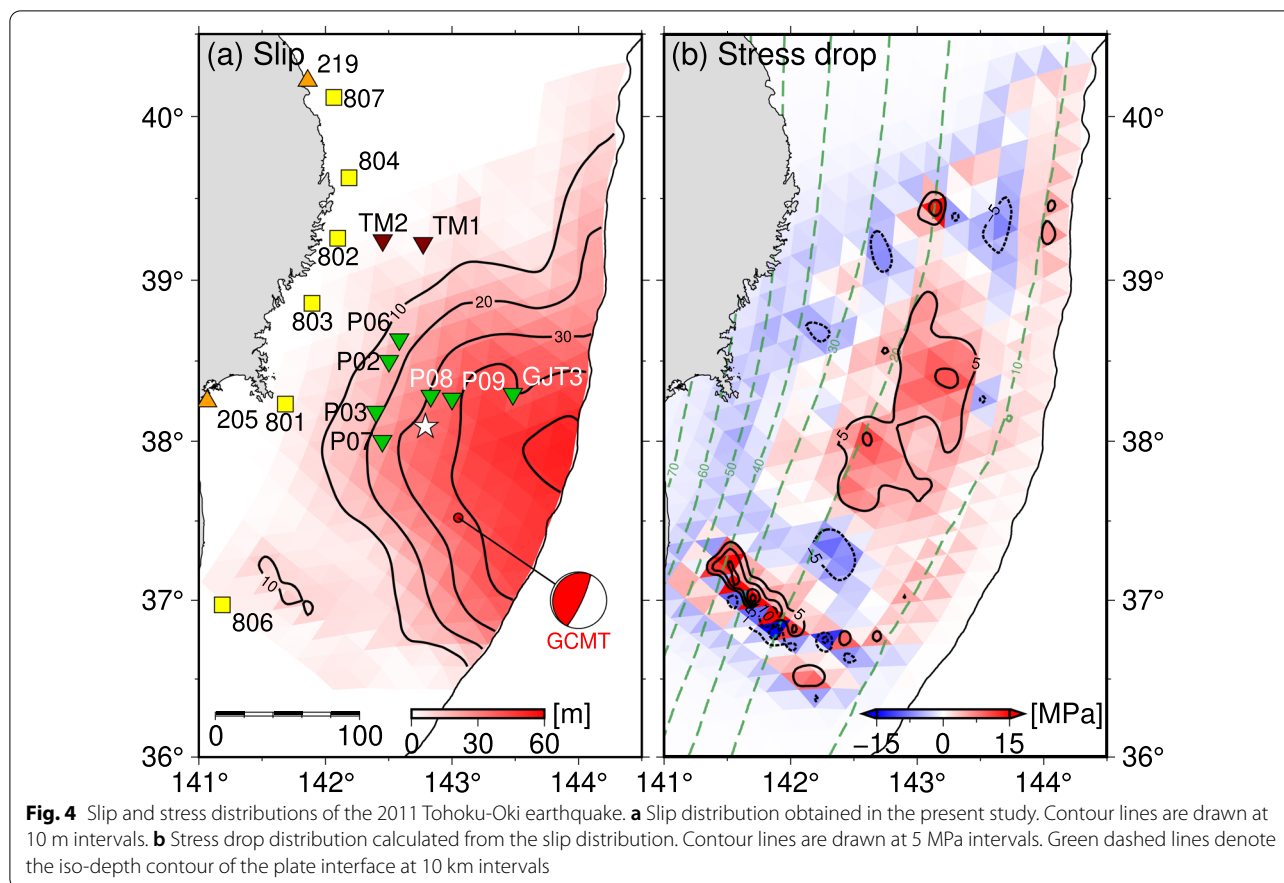
calculated from a vector normal to the subfault surface (i.e., fault-normal vector) $\bar{\mathbf{n}}$ (e.g., Aki and Richards (2002); the schematic illustration is shown in Fig. 3). The rake angles at each subfault are defined based on the direction of the plate convergence (azimuth of 290°, DeMets et al. 2010, Fig. 2d), so that the horizontal component of the slip vector ($\bar{\mathbf{s}}$) has an opposite direction to the relative plate convergence direction (Fig. 3).

2.2.2 Observation equation to be solved

We here describe the procedure to estimate the slip and stress drop distributions along the plate interface (Fig. 4). The procedure is similar to that used in our previous study (Kubota et al. 2021) (refer to Text S1 in Additional file 1 for more detailed information). Considering that the observed data are expressed by the linear superposition of Green’s function, we estimate the amount of slip at each of the triangular subfaults by solving the following observation equation:

$$\begin{pmatrix} w_{\text{tsun}} \mathbf{d}_{\text{tsun}} \\ w_{\text{geod}} \mathbf{d}_{\text{geod}} \\ 0 \\ 0 \end{pmatrix} = \begin{pmatrix} w_{\text{tsun}} \mathbf{G}_{\text{tsun}} \\ w_{\text{geod}} \mathbf{G}_{\text{geod}} \\ \alpha \mathbf{S} \\ \beta \mathbf{E} \end{pmatrix} \mathbf{m}. \tag{1}$$

The vector \mathbf{d} is the data vector, consisting of the observed data, and \mathbf{G} is the matrix consisting of Green’s functions (the synthetics by the unit slip of the subfault). The subscripts denote the types of datasets. The scalar value w denotes the weight of each dataset (see Sect. 2.2.4 for the choice of the weight value). Vector \mathbf{m} consists of the slip amount of the triangular subfaults, which is to be estimated. To stabilize the solution, we impose the smoothing constraint (Maerten et al. 2005) expressed by matrix \mathbf{S} and the damping constraint using the identity matrix \mathbf{E} . Parameters α and β are the weights of each constraint. We set $\alpha=2$ and $\beta=0.1$ for the main results, but we



will discuss its appropriateness in Discussion section (Sect. 4.1.1).

2.2.3 Calculation of the Green's Functions

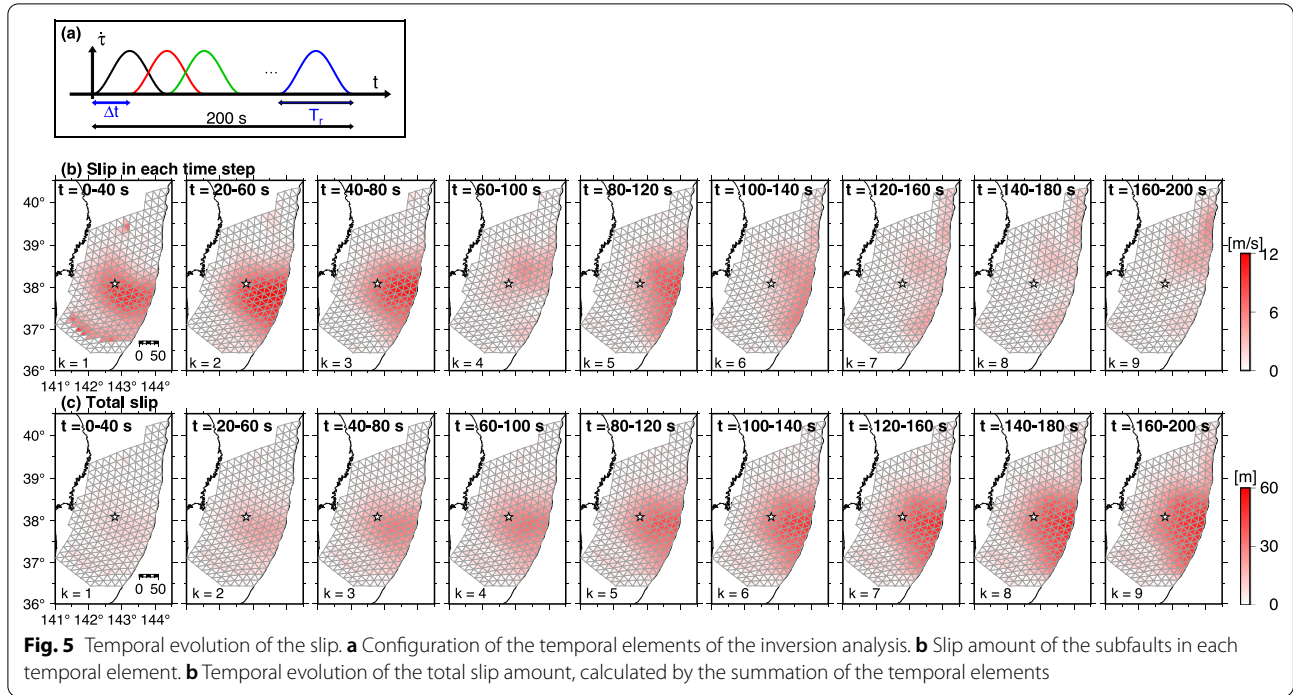
We present the procedure to calculate Green's functions for tsunamis (matrix \mathbf{G}_{tsun} in Eq. (1)) and geodetic data (\mathbf{G}_{geod}) (See Additional file 1: Text S2 for more detail). First, the seafloor vertical displacement distribution from each of the triangular subfaults is simulated using the elastic dislocation theory with the half-space (Meade 2007). The slip direction of each subfault is confined to be the direction of the slip vector schematically shown by red arrow in Fig. 3 (i.e., rake-parallel). We also incorporate the effect of the apparent seafloor vertical movement due to the horizontally moving seafloor (Tanioka and Satake 1996). We then calculate the sea-surface height change from the seafloor deformation using a spatial smoothing filter related to the seawater as the initial condition of the tsunami simulation (e.g., Kajiura 1963; Saito 2019). This filter cuts off the small-wavenumber or spatially short-wavelength component, leading to a smoother initial sea-surface height distribution. We assume a constant depth of $H_0 = 6$ km for this filter, based on the average water depth around the main rupture

region. Finally, we simulate tsunamis using the linear dispersive equation (e.g., Saito 2019), by numerically solving the equation on the discretized staggered grid. The cosine-shaped source time function with the duration of $T_r = 40$ s is assumed for the rupture time history of each subfault, as used in Kubota et al. (2021). In this simulation, the bathymetry data of GEBCO 2020 are interpolated to 2 km spatial intervals. The time interval for this simulation is 1 s. In the calculation of the ocean-bottom pressure gauge waveforms, we incorporate not only the pressure change due to the tsunami (sea-surface height change) but also the static pressure changes related to the seafloor permanent displacement (Tsushima et al. 2012). We finally apply the same low-pass or band-pass filters to the simulated waveforms, as those applied to the observed data.

Green's functions for the geodetic data (\mathbf{G}_{geod}) are also calculated from each of the triangular subfaults, in a similar way to the calculation of the seafloor displacement (Meade 2007).

2.2.4 Solving the Observation Equation

In the linear inversion analysis, we consider the spatial and temporal evolution of the rupture by distributing the



Green’s function in the time domain in addition to the space domain (Fig. 5a). We distribute the Green’s functions in the time domain for each subfault with the temporal interval of $\Delta t = 0.5 \times T_r = 20$ s. The slip of the k -th temporal element begins at $t = t_k^{\text{beg}} = (k - 1) \times \Delta t$ and ends at $t = t_k^{\text{end}} = t_k^{\text{beg}} + T_r$. We assume $N_t = 9$ Green’s functions in the time domain for each subfault. The total number of unknown parameters, which compose the vector \mathbf{m} in Eq. (1), is $N = N_{\text{sub}} \times N_t = 3906$. Considering the rupture front propagation, the slips of the k -th temporal element at the i -th subfault are constrained to be zero when the rupture front does not arrive there (i.e., we allow the slip only when satisfying the condition $V_r \times t_k^{\text{end}} \geq a_i$, where a_i is the distance between the hypocenter and the center of the i -th subfault and $V_r = 4$ km/s is the rupture velocity).

By solving the least squares problem expressed as Eq. (1), using the nonnegative least squares inversion method (Lawson and Hanson 1995), we estimate the spatiotemporal evolution of the slip of the subfaults (vector \mathbf{m} in Eq. (1)). The time windows used for this inversion analysis are shown in the blue traces in Fig. 6a–d. We use the time series data with 1-s sampling (i.e., approximately 1800 to 3600 samples per station), and hence, the total number of the tsunami data sample (\mathbf{d}_{tsun}) is $\sim 10^5$. The offshore and onshore geodetic stations used for the inversion are shown in Fig. 1c, which have three components per station (two horizontal and one vertical), resulting in the total geodetic data samples (\mathbf{d}_{geod}) of $\sim 10^3$. We set

the relative weight of the tsunami and geodetic dataset as $w_{\text{tsun}} = 1$ and $w_{\text{geod}} = 10$, although the actual relative weight is much larger in the tsunami data than the geodetic data, due to the difference of the total data samples. The weights of the spatial smoothing and damping constraints (parameters α and β) are set as $\alpha = 2$ and $\beta = 0.1$, based on the previous modeling results (Kubota et al. 2021) and based on additional inversion analyses assuming various α and β values (discussed later, in Sect. 4).

2.2.5 Variance Reduction

To evaluate the goodness of the waveform fitting between the observation and simulation, we introduce the variance reduction (VR) expressed as follows:

$$\text{VR} = \left[1 - \frac{\sum_i (d_i^{\text{obs}} - d_i^{\text{cal}})^2}{\sum_i (d_i^{\text{obs}})^2} \right] \times 100(\%), \quad (2)$$

where d_i^{obs} is the i -th data of the observed data (vector \mathbf{d}_{tsun} in Eq. (1)) and d_i^{cal} is the calculated one. To calculate the VR, the same time window as that used for the inversion analysis is used (marked by blue lines in Fig. 6a–d).

2.2.6 Calculation of Stress Drop Distribution

After estimating the slip distribution of the triangular subfaults, we calculate the distribution of the shear stress change along the fault (i.e., stress drop, Fig. 4b) by computing the shear stress change along the slip direction at

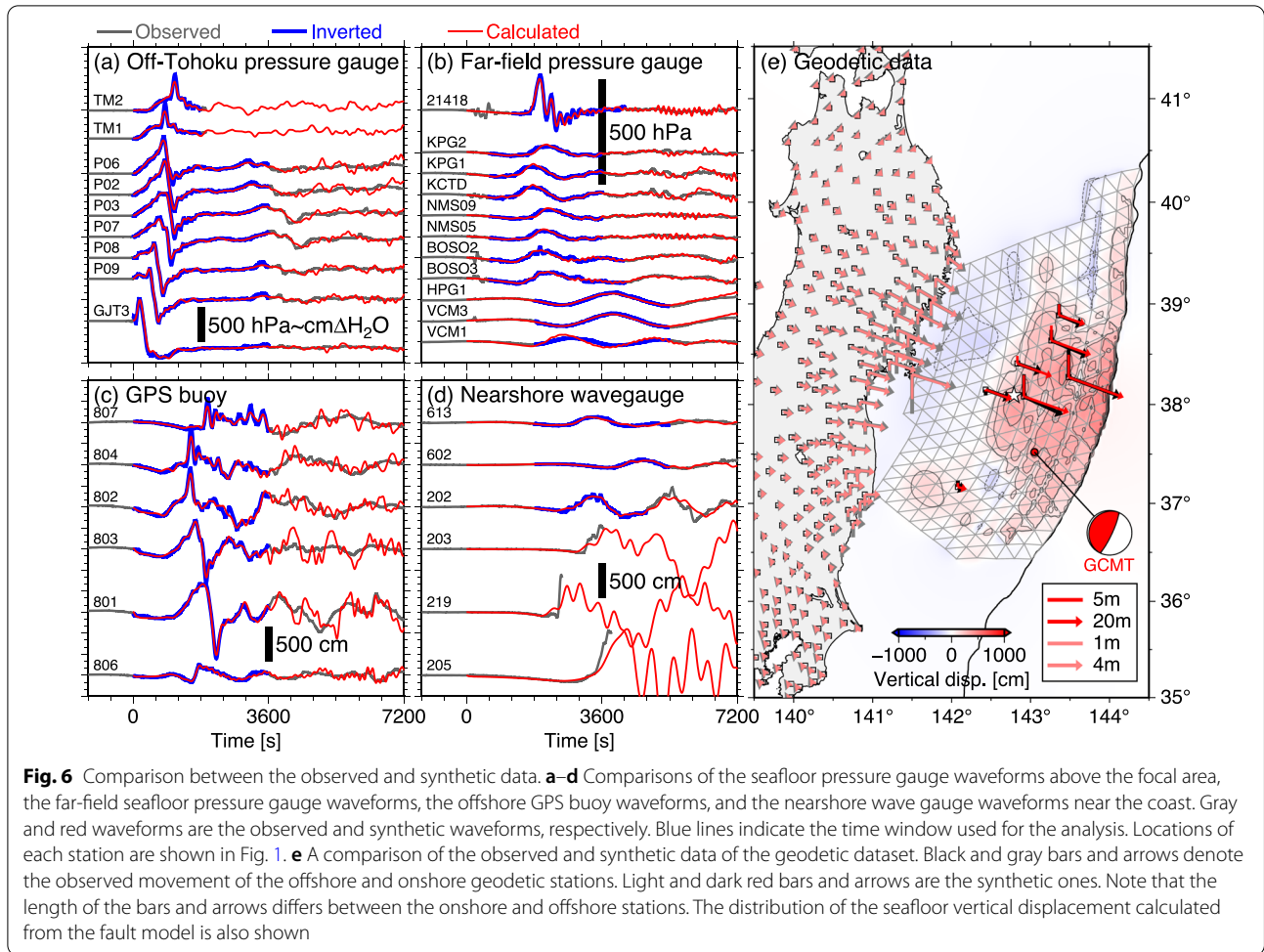


Fig. 6 Comparison between the observed and synthetic data. **a–d** Comparisons of the seafloor pressure gauge waveforms above the focal area, the far-field seafloor pressure gauge waveforms, the offshore GPS buoy waveforms, and the nearshore wave gauge waveforms near the coast. Gray and red waveforms are the observed and synthetic waveforms, respectively. Blue lines indicate the time window used for the analysis. Locations of each station are shown in Fig. 1. **e** A comparison of the observed and synthetic data of the geodetic dataset. Black and gray bars and arrows denote the observed movement of the offshore and onshore geodetic stations. Light and dark red bars and arrows are the synthetic ones. Note that the length of the bars and arrows differs between the onshore and offshore stations. The distribution of the seafloor vertical displacement calculated from the fault model is also shown

the center of each subfault (Saito and Noda 2022). The shear stress change $\Delta\sigma_i(\mathbf{x}_i)$, at the i -th triangular subfault, in which its center is located at \mathbf{x}_i , is expressed by a superposition of the shear stress change contributions by the fault slip of all the subfaults:

$$\Delta\sigma_i(\mathbf{x}_i) = \sum_j \Delta S(\mathbf{x}_i; \mathbf{x}_j) m_j, \quad (3)$$

where m_j is the slip amount at the j -th subfault (located at \mathbf{x}_j), and $\Delta S(\mathbf{x}_i; \mathbf{x}_j)$ is the shear stress change at the center of the i -th subfault caused by the unit slip of the j -th subfault. We define the direction of the shear stress of each subfault based on the fault-normal and slip vectors shown in Fig. 3. Using the unit fault-normal vector $\bar{\mathbf{n}}(\mathbf{x}_i)$ and the unit slip vector $\bar{\mathbf{s}}(\mathbf{x}_i)$ at the i -th subfault, $\Delta S(\mathbf{x}_i; \mathbf{x}_j)$ is calculated as (e.g., Saito and Noda 2022):

$$\Delta S(\mathbf{x}_i; \mathbf{x}_j) = \bar{\mathbf{s}}(\mathbf{x}_j) \cdot \boldsymbol{\tau}(\mathbf{x}_i; \mathbf{x}_j) \bar{\mathbf{n}}(\mathbf{x}_i), \quad (4)$$

where $|\bar{\mathbf{s}}(\mathbf{x}_j)| = 1$ and $|\bar{\mathbf{n}}(\mathbf{x}_i)| = 1$, and $\boldsymbol{\tau}(\mathbf{x}_i; \mathbf{x}_j)$ is the stress tensor at the center of the i -th subfault element caused by

the unit slip of the j -th subfault. We calculate the stress tensor $\boldsymbol{\tau}(\mathbf{x}_i; \mathbf{x}_j)$ using the half-space media (Meade 2007) assuming the rigidity of 40 GPa.

3 Results

3.1 Fault slip distribution

We obtain a large slip of 53 m to the trench axis in the region off Miyagi (approximately at 38.0°N, 144.0°E, Fig. 4a). The seismic moment is $M_0 = 5.07 \times 10^{22}$ Nm (M_w 9.07, assuming a constant rigidity of 40 GPa). In Fig. 5b and c, we show the subfault slip amounts in each temporal element ($k = 1, 2, \dots, N_t$). At the initial stage, $t \leq 80$ s from the rupture initiation, we observe relatively large slip around the hypocenter. Then, the rupture extends to the trench axis until $t = 140$ s. At the later part of the rupture ($t > 140$ s), we observe the rupture at the near-trench area of the northern part, off-Sanriku, Iwate, region ($\sim 39.5^\circ\text{N}$). This spatiotemporal evolution of the rupture is consistent with that estimated from the seismogram analyses in the past studies (e.g., Ide et al. 2011). The synthetic tsunami (Fig. 6a–d)

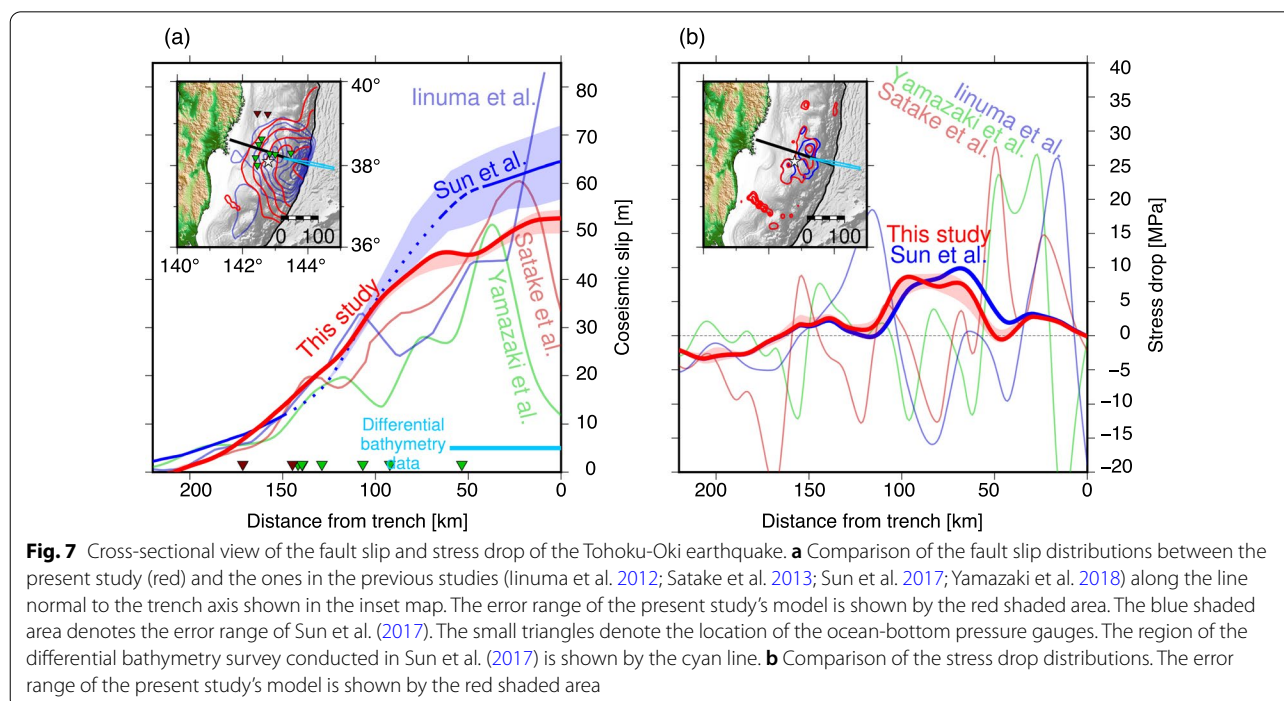
and onshore and offshore displacement (Fig. 6e) from this slip distribution model are in good agreement with the observations ($VR=97.7\%$). The main slip area, defined as the region where the slip exceeded 10 m, is consistent with that reported previously (e.g., Iinuma et al. 2012; Satake et al. 2013; Yamazaki et al. 2018).

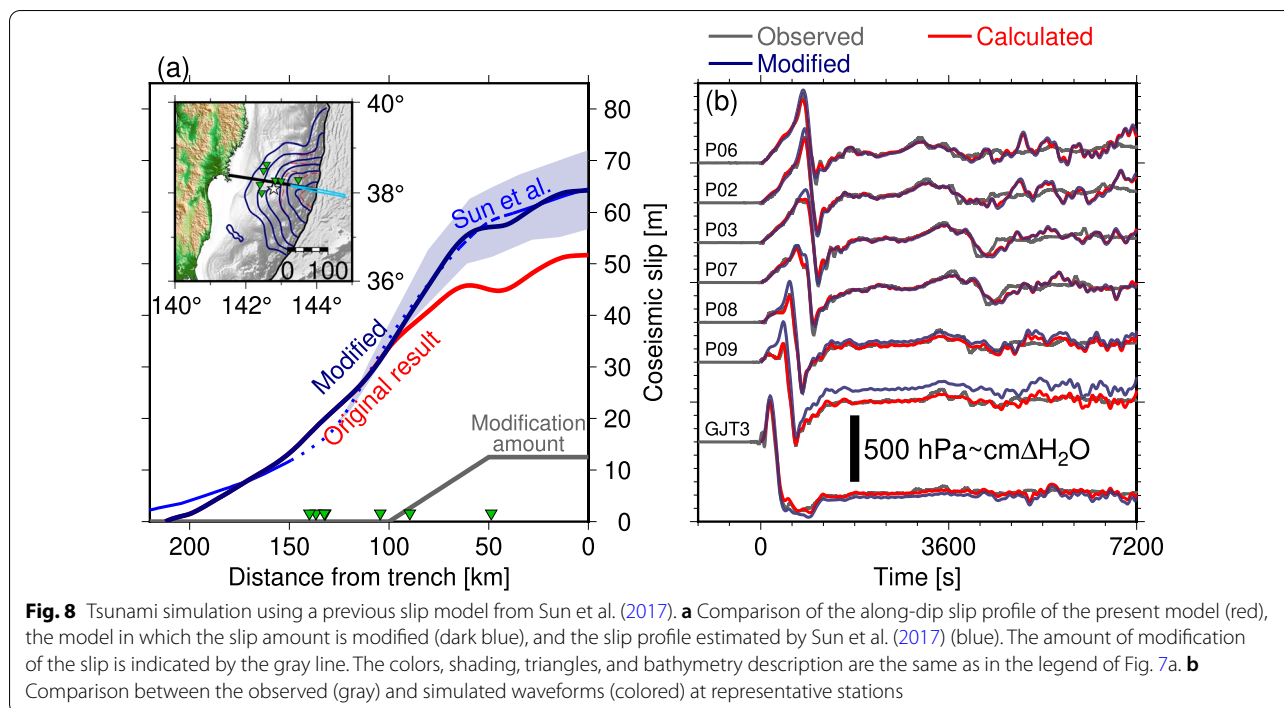
We evaluate the uncertainty of the slip estimation by additional inversion tests based on a jack-knife approach (Additional file 1: Figure S1a and red shaded area in Fig. 7a). In this test, we exclude one of the nine near-field pressure gauge stations (Fig. 6a) and use the remaining eight stations to estimate the slip distribution. The inversion setting is identical to the original setting which used all the data. We define the possible range of the slip amount using the maximum and minimum slip amounts from all tested models. As a result, the possible range of the shallowest slip is between 49 and 55 m at the Off-Miyagi region (red shaded area in Fig. 7a).

Our model has a peak slip at the trench axis (red line in Fig. 7a), which is consistent with the study by Sun et al. (2017) who estimated the near-trench slip profile of the Off-Miyagi region using the bathymetry change based on the surveys conducted before and after the Tohoku-Oki earthquake (blue line in Fig. 7a). In contrast, other previous models (e.g., Yamazaki et al. 2018) locate the peak slip a few tens of kilometers from the trench axis (green line in Fig. 7a). The gradient of the slip along the dip direction is also consistent with that of Sun et al. (2017).

The slip amount at the trench axis in our study is slightly smaller (~ 53 m) than that of Sun et al. (2017) (~ 65 m), by ~ 12 m. Therefore, we examine whether the slip profile reaching up to 65 m, estimated by Sun et al. (2017), can explain the tsunami waveform observed by the near-field pressure gauges (Fig. 8). Because the coseismic slip estimated by Sun et al. (2017) was available only at the near-trench region, our slip distribution model is used as a reference to emulate the slip model of Sun et al. (2017) (see Text S3 for the detailed procedure). As a result, the simulated tsunami waveforms are almost consistent with the observation ($VR=95.7\%$), but the peak amplitudes at the stations near the epicenter (P08 and P09) are larger than those observed (Fig. 8b). This may indicate that the maximum slip near the trench is not as large as 65 m.

We also examine how the near-field ocean-bottom pressure data that we newly used contribute to the improvement of the modeling resolution, by conducting tsunami simulations using the previous slip distributions of Satake et al. (2013), Iinuma et al. (2012), and Yamazaki et al. (2018) (Fig. 9, see Text S4 for the detailed simulation procedure). The model of Iinuma et al. (2012) has an extremely large slip at the trench (light blue line in Fig. 7a), which produces a short-wavelength tsunami inconsistent with the observations (stations P03, P07). The model of Yamazaki et al. (2018) has the maximum slip located at ~ 40 km inboard of the trench (green line), which produces





the larger short-wavelength tsunami than the observation at GJT3. We quantify the goodness of the slip models based on the VR value (Eq. (2)) using the time window of 0 to 1800s from the near-field seven pressure gauge waveforms (P02, P03, P06, P07, P08, P09, and GJT3, hereafter referred to as VR_{near}). We obtain $VR_{\text{near}} = 65.4\%$ for the model of Satake et al. (2013), $VR_{\text{near}} = 5.5\%$ for Iinuma et al. (2012), and 35.7% for Yamazaki et al. (2018), while our fault model obtains $VR_{\text{near}} = 99.2\%$. The fault models of these previous studies cannot explain the near-field ocean-bottom pressure gauges waveforms, which indicates that the use of the near-field tsunami data obtained by the pressure gauges contributes to revealing the detailed shallow slip profile at the trench.

3.2 Stress drop

We show the shear stress change along the fault plane (i.e., the stress drop) in Fig. 4b. The stress release at the deep portion (> 10 km) is large (> 5 MPa), where the slip amount is smaller than ~ 40 m, whereas the stress release at the shallowest portion ($> \sim 40$ m slip) is much smaller.

Similar to the slip uncertainty evaluation, we evaluate the stress drop uncertainty based on the jack-knife approach (Additional file 1: Figure S1b, red shaded area in Fig. 7b). We calculate the stress drop distribution based on the slip distribution models estimated by excluding one of the nine near-field pressure gauges. The possible range of the stress drop is then defined by the

maximum and minimum slip amounts from all tested models. Taking the uncertainty of the estimation into account, the stress drop at the shallow portion is smaller than 3 MPa (Additional file 1: Figure S1b and 7b). Considerable stress drop at the deeper portion suggests that a strong mechanical coupling at the deeper portion accumulated the significant amount of shear stress before the earthquake, while insignificant coseismic stress release at the shallow portion suggests much weaker shallow mechanical coupling than the deep portion before the earthquake (discussed later in Sect. 4.2).

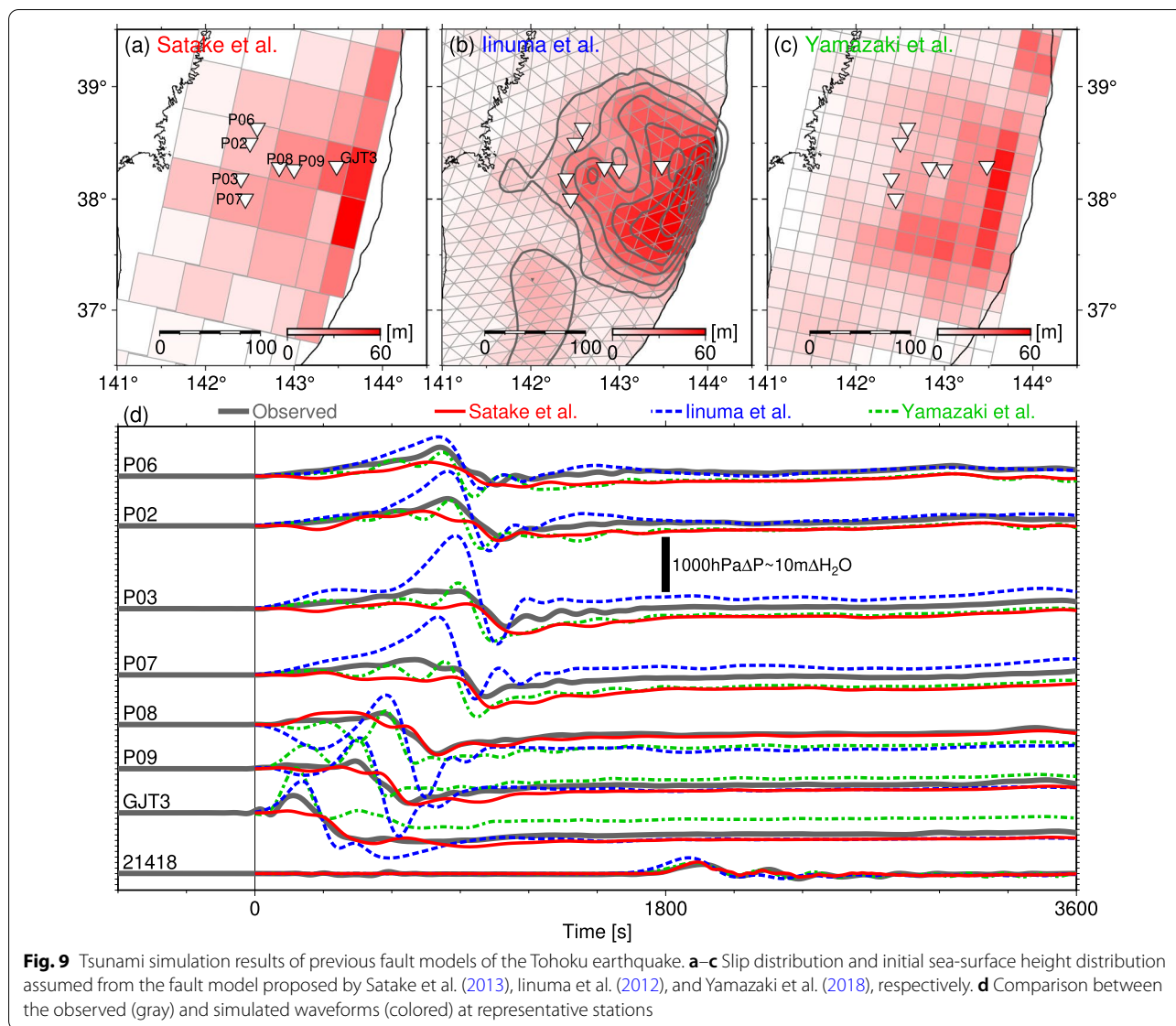
4 Discussion

4.1 Evaluation of estimated fault model

4.1.1 Constraint weights in the inversion analysis

In our inversion analysis, we use the weights of the smoothing and damping constraints of $\alpha = 2$ and $\beta = 0.1$. However, as the slip distribution may be sensitive to these parameters, shear stress change calculation from the slip distribution will be also highly sensitive to the choices of these parameters. Therefore, we conduct additional inversions assuming various constraint weight parameters (Additional file 1: Figures S2–S10).

Our tests of smoothing and damping parameters (Additional file 1: Figures S2–S10) show that the inversions are more sensitive to the smoothing weight α than the damping weight β . When we assume the smaller smoothing constraint ($\alpha = 0.2$, Additional file 1 Figures S2–S4), although the observed waveforms used in the inversion



are reproduced well ($VR > 98\%$), the calculation fails to reproduce the later part of the tsunamis observed GPS buoys not used in the inversion analysis (Additional file 1: Figures S2e, S3e, and S4e). In addition, the slip distributions significantly include short-wavelength heterogeneities and this leads to the extremely large stress drop with finer-scale spatial heterogeneity. This overly rough distributions of slip and stress drop distributions must be artifacts due to the inappropriately smaller smoothing constraint, considering that the tsunami data, which have the dominant period of larger than 100 s, cannot resolve such small-scale heterogeneities. The heterogeneous slip and stress drop distributions related to the smaller smoothing constraint should be arisen from the modeling error, mainly due to the overfitting of the data

which contain various noises such as the observational noises (e.g., Yabuki and Matsu'ura 1992; Fukahata and Wright 2008).

When we impose smoothing constraints equal to or larger than the original value ($\alpha = 2$ or 20, Additional file 1: Figures S5–S10), we basically observe the trench-reaching slip. When supposing the stronger smoothing constraint ($\alpha = 20$, Additional file 1: Figures S8–S10), the amount of the near-trench slip is smaller than the original results (~ 40 m) and the impulsive tsunami components at some stations (e.g., TM1, TM2, 21,418, 807, and 804) could not be reproduced. This means that the smoothing weight of $\alpha = 20$ is inappropriately large. Even though the $\alpha = 20$ models are inappropriate, we note that the stress drop distributions calculated from these

models are similar to the original model, in which the maximum stress drop is located at the deeper portion but no stress release at the shallower portion. Our main results, that the stress release occurred only at the deeper portion, do not change in a possible range of the smoothing constraint.

4.1.2 Robustness of shallow stress drop estimation

Our result suggests that the stress release at the shallowest portion corresponding to the near-trench large slip ($> \sim 40$ m slip) is lower in magnitude than the deep portion (Fig. 4b). Brown et al. (2015) suggested that some past fault models had larger stress drop in the shallow portion than that in the deeper portion (> 30 MPa, e.g., Yamazaki et al. 2018). We here evaluate the exact location

of the main stress drop and examine how insignificant the shallow stress is, based on tsunami forward simulations assuming virtual earthquakes.

We assume large stress drop regions at shallow, deep, and deeper portions of the plate interface, respectively (Fig. 10a–c, shown by thick black lines). We assign a stress drop of 5 MPa in each of the portions, based on the stress drop amount estimated in our inversions (Fig. 4b). Then, assuming the given stress drop amount as the virtual observed data (left-hand side of Eq. (3)), we estimate the slip amount of the j -th subfault (m_j) by solving the linear inversion problem (Noda et al. 2021; Saito and Noda 2022) (contour lines in Fig. 10a–c). Finally, using this virtual fault slip model, we forwardly simulate tsunamis to compare with the pressure gauge waveforms (Fig. 10d).

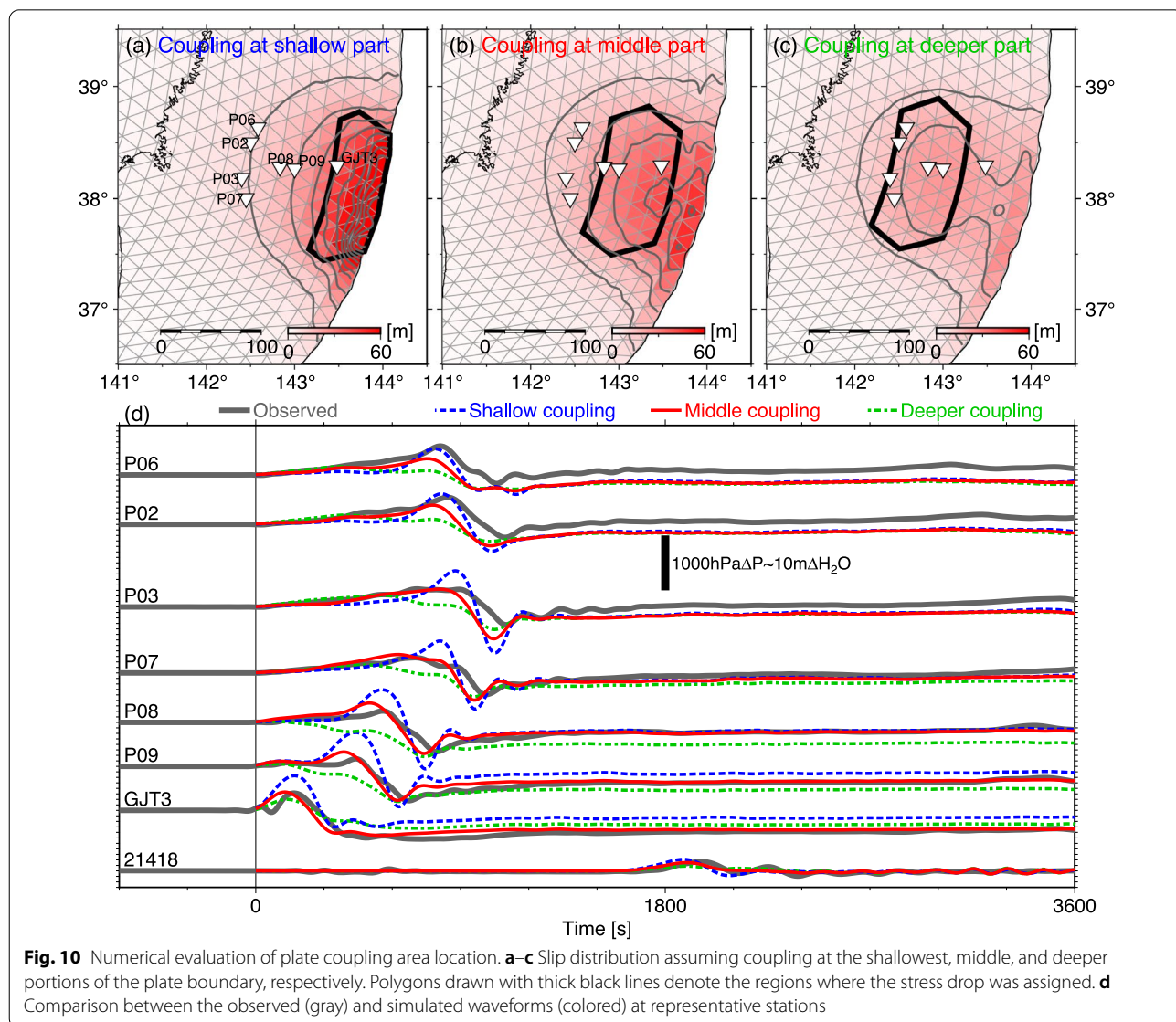
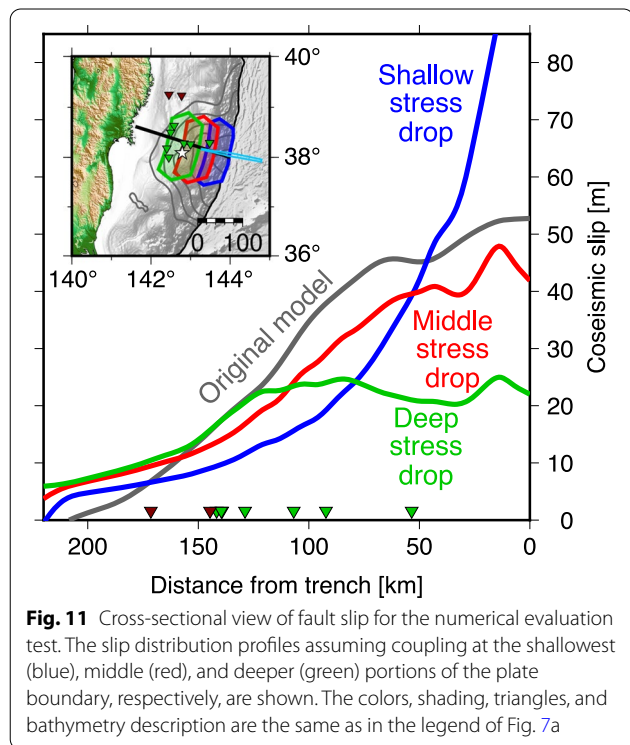


Fig. 10 Numerical evaluation of plate coupling area location. **a–c** Slip distribution assuming coupling at the shallowest, middle, and deeper portions of the plate boundary, respectively. Polygons drawn with thick black lines denote the regions where the stress drop was assigned. **d** Comparison between the observed (gray) and simulated waveforms (colored) at representative stations

The temporal evolution of the fault is assumed so that all the slip across the fault starts simultaneously at $t=0$ and ends after the duration of $T_r=40$ s.

As a result, when assuming a large stress drop area at the deep portion of the plate boundary where the large stress drop was estimated in our modeling (Fig. 10b), we obtain the near-trench slip up to ~ 50 m and a moderate spatial slip gradient consistent with our fault model (red line in Fig. 11). This model explains the features of the observed tsunamis well (red traces in Fig. 10d). On the other hand, when assuming a large stress drop area of 5 MPa at the shallowest portion near the trench (Fig. 10a), a maximum slip of >80 m and a large spatial gradient of the slip amount are necessary to cause the large stress drop at the shallowest portion (blue line in Fig. 11). This shallow extremely large slip generates very large short-wavelength tsunamis but cannot explain the observation (blue traces in Fig. 10d). The ~ 20 m shallow slip based on the assumption of a further deeper stress drop area (Fig. 10c, green line in Fig. 11) cannot explain the observation as well (green traces in Fig. 10d). From these forward simulations, we conclude that the large stress drop area should be located around deeper part of the plate boundary near the hypocenter.

We also examine how insignificant the stress was released in the shallow portion, based on another tsunami forward simulation (Additional file 1: Figure S11). We modify the stress drop distribution of our model



(Fig. 4b) so that the shallow stress drop in the Off-Miyagi region ($\sim 37\text{--}39^\circ\text{N}$) becomes zero (Additional file 1: Figure S11a) and construct the virtual slip distribution with the same procedure as the forward simulations above (Additional file 1: Figure S11b). Using this fault slip distribution, we then simulate tsunamis (Additional file 1: Figure S11c). As a result, the simulation reasonably explains the features of the observed tsunamis well even if we suppose no stress drop in the shallow portion (dark blue traces in Additional file 1: Figure S11c). This result supports that the shallow stress drop is much smaller in magnitude than the deeper portion.

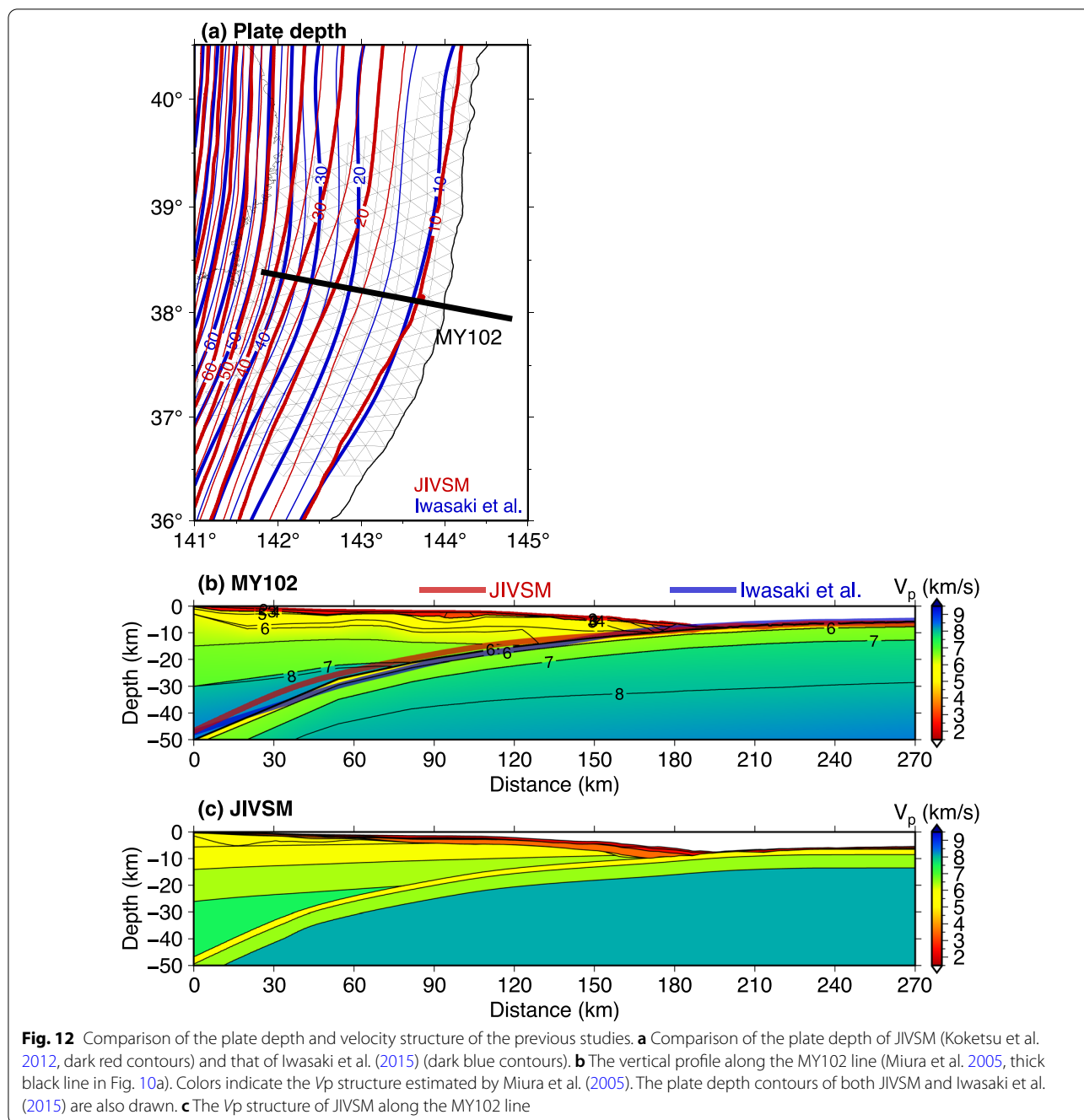
4.1.3 Effects of heterogeneous structure

To check the validity of the use of the JIVSM plate boundary model for the fault modeling, we compare the JIVSM with a plate boundary model of Iwasaki et al. (2015), constructed from the precise seismicity and active survey data (Fig. 12a). We also compare the JIVSM with the V_p structure along the MY102 survey line in the Off-Miyagi region estimated by an air-gun survey (Miura et al. 2005, Fig. 12b). There are some differences between the models, but we confirm the plate depth is reasonably similar to each other at the shallowest portion where the large near-trench slip occurred. This indicates that the use of the plate geometry from the JIVSM is reasonable to estimate the realistic stress drop distribution.

It is possible that the heterogeneity of the crustal structure may affect the calculation of the stress drop (Figs. 12b and c, e.g., Yagi and Fukahata 2011; Fukahata et al. 2012). Because the rigidity at the shallowest portion of the plate boundary should be smaller than that assumed in this study, the stress change at the shallow portion is expected to be smaller than that obtained from our study. Even if the heterogeneity of the structure is considered, we would be able to reasonably state that the shallow stress drop is much less significant than the deeper portion. In the next step, we further consider this heterogeneous crustal structure using the numerical simulation approach (e.g., Ma 2012; Maeda et al. 2017; Sun et al. 2017; Herman et al. 2018; Du et al. 2021). In addition, it will be necessary to consider the seafloor bathymetry, which cannot be incorporated in the half-space calculation (Wang et al. 2018). It will be also important to consider the inelastic deformation effect due to dynamic coseismic stress change, leading to an enhancement of the tsunami (e.g., Ma 2012; Ma and Nie 2019; Du et al. 2021).

4.2 Mechanism of near-trench large slip: kinematic and dynamic perspectives of the fault boundary

The use of the near-field ocean-bottom pressure gauge made it possible to resolve the shallow slip and stress



drop distributions of the Tohoku-Oki earthquake, which shows the shallow stress drop was insignificantly small. In addition, the seafloor drilling survey conducted after the Tohoku-Oki earthquake suggested that the absolute shear stress level after the earthquake at the shallow plate interface was almost zero (Lin et al. 2013; Brodsky et al. 2017; 2020). According to the experimental studies using the shallow fault-zone material of the Tohoku subduction zone (Ujiie et al. 2013; Remitti et al. 2015),

the temperature measurements of the interplate frictional heating due to the earthquake (Fulton et al. 2013), and the seismic active survey study (Hondori and Park 2022), it is suggested that the friction coefficient in the shallow plate interface is considerably low, resulting in very low absolute level of the shear stress. Therefore, it is suggested that the shear stress at the shallow portion should be also nearly zero during, and even before, the Tohoku-Oki earthquake, and the shallow portion did not

accumulate the shear stress during the long-term interseismic period (i.e., no shallow mechanical locking). Based on these results, we propose that the main reason for the large shallow coseismic slip is a stress release of a deeper locked zone, where the stress accumulates during the interseismic period. In other words, the Tohoku-Oki earthquake slip occurred to compensate for the interseismic slip deficit at both deep and shallow parts of the plate interface, which was provoked only by deep mechanical coupling (Fig. 13) (Almeida et al. 2018; Herman et al. 2018). Before the Tohoku-Oki earthquake, it was widely believed that the shallow plate interface does neither accumulate the shear stress (Scholtz 1998; Bilek and Lay 2002) nor the slip deficit (Suwa et al. 2006; Hashimoto et al. 2009; Loveless and Meade 2010; 2011). Our study indicates that the shallow stress accumulation behavior is consistent with that expected before the Tohoku-Oki earthquake, but the slip deficit accumulation behavior is not.

Most previous studies have conventionally understood the occurrence of large earthquakes based on a kinematic perspective (e.g., Nishikawa et al. 2019; Uchida

and Bürgmann 2021) (Fig. 13b). As has been seen in other large earthquakes, the main slip of the Tohoku-Oki earthquake was located in the slip deficit area during the interseismic period (Lindsey et al. 2021), indicating that the earthquake released the interseismic slip deficit. Seismic waves were radiated mainly at deeper depths, but there was almost no radiation at shallow depths (Ide et al. 2011). Afterslips occurred in areas without coseismic slip (Watanabe et al. 2021). Other typical kinematic pictures are shown in Fig. 13b. To explain the extremely large shallow slip which was unusual within this kinematic perspective, some studies considered the possibility of an additional mechanism causing an extensive dynamic reduction of friction, such as thermal pressurization, which results in an extremely large stress drop process at the shallow part (Hirono et al. 2019; Shibazaki et al. 2019).

Here, based on the data analysis focusing on the stress drop distribution, we expanded this kinematic view to a new mechanical picture (Fig. 13a). From a mechanical perspective, the rupture area of the Tohoku-Oki earthquake can be divided into deeper (>~10 km) and

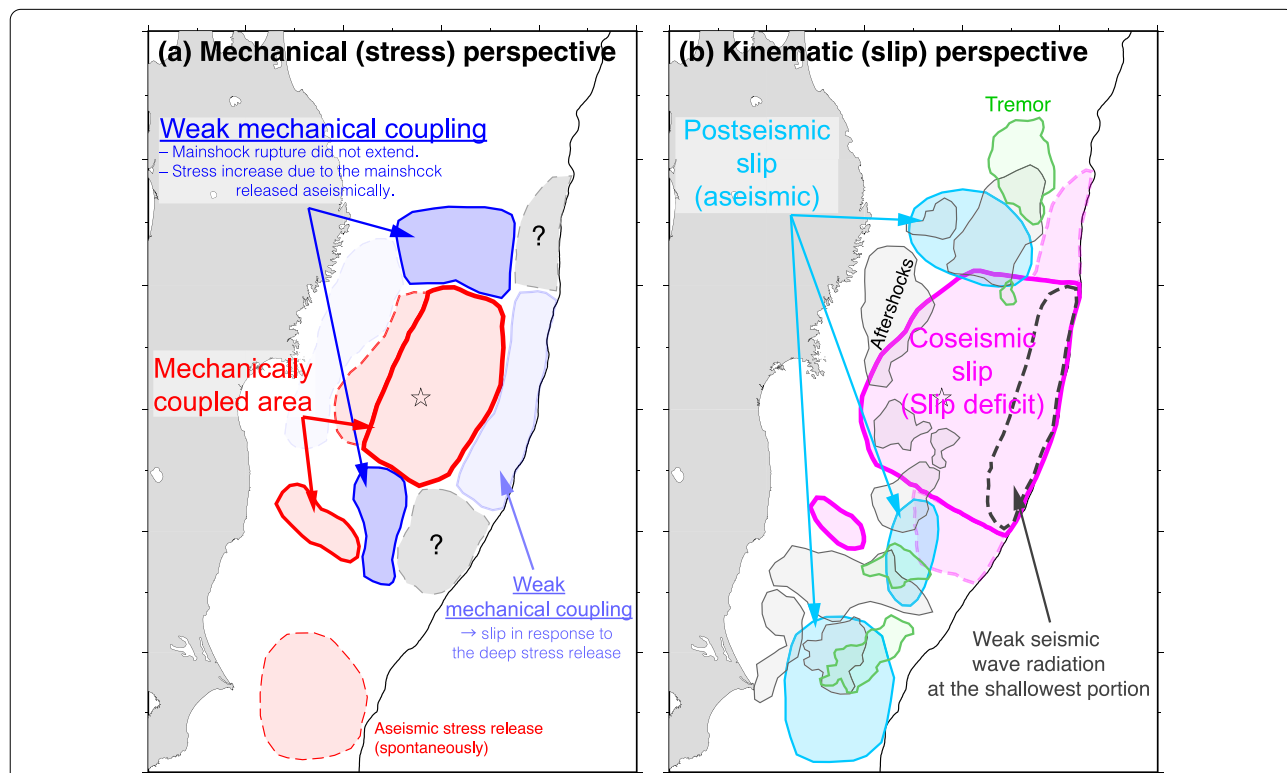


Fig. 13 Interpretation of the mechanical and kinematic properties along the Tohoku plate boundary. **a** Mechanical perspective associated with the megathrust Tohoku-Oki earthquake. The regions where the plate boundary is mechanically locked are shown in red, and the regions where the mechanical coupling is weak are shown in blue. The regions surrounded by dashed lines are less certain than those with the solid lines. The regions where the mechanical property is unclear are shown in gray. **b** Kinematic perspective of the seismic activities along the plate boundary. The spatial relationship of the coseismic (magenta) and postseismic (cyan) slips are shown. Aftershock areas are also shown in gray, and tremor areas are shown in green

shallower ($< \sim 10$ km) portions. We propose that the driving force of the entire slip was the accumulated strain energy at the deep mechanically coupled area. The amount of shallow slip seemed incredibly large, but it can be reasonably interpreted by considering the effect of the deep stress release and its interaction with the free surface (Almeida et al. 2018; Herman et al. 2018). In addition, a large seismic wave radiation area is well correlated with the area of the large stress drop, whereas the shallow weak seismic wave radiation area corresponds to the low stress drop area.

Although the kinematic concept of afterslips is simple and complementary to the main shock (Watanabe et al. 2021), we propose two different mechanisms of afterslip: The afterslips located just north ($\sim 39.5^\circ\text{N}$) and south ($\sim 37^\circ\text{N}$) of the rupture area were driven to dissipate stress concentration due to the mainshock, while the slip which occurred ~ 200 km south ($\sim 35.5^\circ\text{N}$) was not directly driven by the stress concentration, but it spontaneously started (i.e., triggered aseismic slip).

4.3 Toward understanding of the Tohoku-Oki earthquake and megathrust earthquake physics

In addition to the conventional kinematic perspective of the megathrust earthquake, the stress drop distribution provided us with additional information about the megathrust earthquake, including the cause of the driving force that triggered the shallow large slip, the source of seismic wave excitation, and the existence of different types of afterslip generation mechanisms (Fig. 13). These observations are consistent with the basic mechanical model of faulting (Kostrov 1974), in which the strain energy stored in the lithosphere between the interseismic period excites the fault slip and seismic wave radiation. Without assuming any special mechanism requiring an extremely large shallow stress drop, the anomalous shallow slip can be explained by a combination of free surface and deep stress release (Fukuyama and Hok 2015; Almeida et al. 2018; Herman et al. 2018).

The large shallow slip of the Tohoku-Oki earthquake was mainly due to the effect of the free surface and the deep stress release (Almeida et al. 2018; Herman et al. 2018). This indicates that the shallow slip behavior depends largely on the location and amount of the stress drop. More specifically, the earthquake slip behavior relies on the amount of strain energy accumulated around the mechanically coupled area. The rupture of the M_w 7.2 foreshock on 9 March 2011, which preceded the Tohoku-Oki earthquake by two days, had a much smaller stress drop of 1.0 MPa on average (Kubota et al. 2017), resulting in a smaller amount of the released strain energy as compared to the March 11 mainshock. Although we

need further efforts to deepen our understanding of the mechanics of the foreshock and the mainshock, the difference in the amounts of the strain energy released by these earthquakes would be essentially important to understand the diversity of the earthquake dynamics.

The past studies using the onshore geodetic data suggested that there were no interplate slip deficits in the shallowest portion of the plate interface (Suwa et al. 2006; Hashimoto et al. 2009; Loveless and Meade 2010; 2011), leading to no shallow large seismic slip. However, recent studies suggest interplate slip deficits have been geodetically detected even in the shallowest portion of the plate in many subductions (e.g., Loveless and Meade 2015; Noda et al. 2018; Herman and Govers 2020; Lindsey et al. 2021). Our results show that unusually large shallow slips and giant tsunamis such as those occurring due to the Tohoku-Oki earthquake can occur in any subduction zones even without a shallow stress release, if enough strain energy is accumulated to generate earthquakes around the locked portion which is commonly thought to be at the seismogenic depth (> 10 km). This idea requires methods to evaluate whether enough shear stress or strain energy is accumulated or not around the deeper locked areas which can generate large coseismic slips during the anticipated megathrust earthquakes in the future. For example, some studies assess the potentials of future megathrust earthquakes by evaluating the energy budget associated with the earthquake faulting based on the detected mechanically coupled distributions along the plate interface (Noda et al. 2021; Saito and Noda 2022). Our results showed that observational earthquake science is steadily progressing from kinematic modeling toward mechanical modeling to achieve quantitative evaluation.

5 Conclusions

To understand the reason for the large near-trench slip during the 2011 Tohoku-Oki earthquake, this study estimated the slip and stress drop distributions with the high spatial resolution using the tsunami data recorded by ocean-bottom pressure gauges installed above the fault area, which had not before been used in the past. The estimated model had a large slip of > 40 m at the shallowest portion ($z < 10$ km) in the Off-Miyagi region and the slip peaked at 53 m at the Japan Trench. However, the stress release at the shallowest portion was insignificantly small (< 3 MPa). The main stress drop region (> 5 MPa) was located at the deep portion (> 10 km) where the slip amount was smaller than ~ 40 m. The results suggested the deep mechanical plate locking corresponding to the large stress drop provoked the interseismic slip deficit in both shallow and deep regions of the plate boundary. Although a large shallow slip had been considered as a

result of the release of large strain energy in the shallow portion of the plate boundary in the past, our analyses provided us with a new mechanical perspective along the plate boundary, in which shallow slips can occur without the shallow energy accumulation but only with the energy accumulation in the deeper portion.

Abbreviations

DART: Deep-ocean Assessment and Reporting of Tsunamis; GSI: Geospatial Information Authority of Japan; JAMSTEC: Japan Agency for Marine-Earth Science and Technology; JIVSM: Japan Integrated Velocity Structure Model; JMA: Japan Meteorological Agency; JPL: Jet Propulsion Laboratory; NASA: National Aeronautics and Space Administration; NIED: National Research Institute for Earth Science and Disaster Resilience; NOAA: National Oceanic and Atmospheric Administration; NOWPHAS: Nationwide Ocean Wave information network for Ports and Harbours; PARI: Port and Airport Research Institute.

Supplementary Information

The online version contains supplementary material available at <https://doi.org/10.1186/s40645-022-00524-0>.

Additional file 1. Supplementary Texts and Figures. This file includes Texts S1 to S4, Figures S1 to S11, and the detailed captions for Datasets S1 to S6.

Additional file 2. Dataset S1. Comma-separated CSV file for the locations of tsunami stations used in this study.

Additional file 3. Dataset S2. Comma-separated CSV file for the locations of the geodetic stations used in this study.

Additional file 4. Dataset S3. Text file for slip amounts of each subfault estimated by the present study.

Additional file 5. Dataset S4. NetCDF grid file for final slip distribution interpolated from the slip amounts of each subfault.

Additional file 6. Dataset S5. Text file for stress drops of each subfault calculated from the slip distribution model.

Additional file 7. Dataset S6. NetCDF grid file for stress drop distribution interpolated from the stress drop amount of each subfault.

Acknowledgements

We thank two anonymous reviewers and the Editor Takeshi Iinuma for their reviews and insightful comments. The figures in this manuscript were prepared using Generic Mapping Tools (GMT) version 6 (Wessel et al. 2019). We also thank Editage for the English language review.

Author contributions

TK conducted the analyses and numerical experiments described in this paper. TS and RH interpreted the results. All authors drafted the manuscript. All authors read and approved the final manuscript.

Funding

This work was financially supported by JSPS KAKENHI Grant Numbers JP19H02409 (TK, TS), JP19H05596 (RH), JP19K04021 (TS), JP19K14818 (TK), and JP22K22K14126 (TK).

Availability of data and materials

The ocean-bottom pressure gauge data installed by Tohoku University are available in the supplementary data of Kubota et al. (2021), at <https://doi.org/10.5281/zenodo.4420393>. DART tsunami data were downloaded from https://www.ngdc.noaa.gov/hazard/dart/2011honshu_dart.html (accessed on 1 September 2022). The tsunami data of JAMSTEC were downloaded from http://www.jamstec.go.jp/scdc/top_e.html (accessed on 1 December 2019 but currently unavailable on 1 September 2022). The pressure data of the JMA are available in the supplementary data of Technical Report of the Japan Meteorological Agency Vol. 1 "3 Report on the 2011 Off the Pacific Coast of

Tohoku Earthquake" (https://www.jma.go.jp/jma/kishou/books/gizyutu/133/gizyutu_133.html, accessed on 1 September 2022, available only in Japanese). The NIED pressure gauge data were provided on request. The tsunami data of the nearshore GPS buoy and wave gauges were downloaded from the NOWPHAS webpage (<https://nowphas.mlit.go.jp/pastdata/>, only available in Japanese, accessed on 1 September 2022). The coseismic displacements at offshore geodetic stations (Kido et al. 2011; Sato et al. 2011) are listed in Iinuma et al. (2012). The coseismic displacement data at the onshore geodetic stations were downloaded from the website of Jet Propulsion Laboratory (JPL), National Aeronautics and Space Administration (NASA) (<https://gipsy-oasis.jpl.nasa.gov/index.php?page=pppdata>, accessed on 1 September 2022), which were originally acquired by the GSI. The Japan Integrated Velocity Structure Model (Koketsu et al. 2012) was downloaded from https://www.jishin.go.jp/evaluation/seismic_hazard_map/psmh/12_choshuki_dat/ (accessed on 1 September 2022, available only in Japanese). Plate boundary model of Iwasaki et al. (2015) (Fig. 12) was downloaded from http://evrrss.eri.u-tokyo.ac.jp/database/PLATEmodel/PLMDL_2016/, and the readme file is available at http://evrrss.eri.u-tokyo.ac.jp/database/PLATEmodel/PLMDL_2016/README_en.pdf (accessed on 1 September 2022). The two-dimensional V_p structure model along the MY102 line (Fig. 12, Miura et al. 2005, https://www.jamstec.go.jp/obsrms_db/e/survey/data_area.html?cruise=KY99-05) was provided by JAMSTEC upon request via JAMSTEC Seismic Survey Database (JAMSTEC 2004, <https://doi.org/10.17596/0002069>; https://www.jamstec.go.jp/obsrms_db/e/). The GEBCO 2020 bathymetry data were downloaded from https://www.gebco.net/data_and_products/historical_data_sets/#gebco_2020 (accessed on 1 September 2022). We used a triangular dislocation element (tde) program (Meade 2007, <https://github.com/brendanmeade/tde>) to calculate seafloor deformation (accessed on 1 September 2022). The digital data of the slip distribution and stress drop estimated by this study are available in Additional files 2–7: Datasets S1 to S6 and the detailed caption of the dataset are shown in Additional file 1. The dataset is also available at the external data repository Zenodo (<https://doi.org/10.5281/zenodo.7104297>).

Declarations

Competing interests

The authors declare that they have no competing interest.

Author details

¹National Research Institute for Earth Science and Disaster Resilience, 3-1 Tennodai, Tsukuba, Ibaraki 305-0006, Japan. ²Graduate School of Science, Tohoku University, 6-6 Aza-Aoba, Aramaki, Aoba-Ku, Sendai, Miyagi 980-8578, Japan.

Received: 2 June 2022 Accepted: 17 November 2022

Published online: 05 December 2022

References

- Aki K, Richards PG (2002) Quantitative seismology, 2nd edn. University Science Books, Mill Valley, CA
- Almeida R, Lindsey EO, Bradley K, Hubbard J, Mallick R, Hill EM (2018) Can the updip limit of frictional locking on megathrusts be detected geodetically? Quantifying the effect of stress shadows on near-trench coupling. *Geophys Res Lett* 45:4754–4763. <https://doi.org/10.1029/2018GL077785>
- Bilek SL, Lay T (2002) Tsunami earthquakes possibly widespread manifestations of frictional conditional stability. *Geophys Res Lett* 29:1673. <https://doi.org/10.1029/2002GL015215>
- Brodsky EE, Saffer FP, Chester CM, Huffman K, Moore JC, Wu H-Y (2017) The postearthquake stress state on the Tohoku megathrust as constrained by reanalysis of the JFAST breakout data. *Geophys Res Lett* 44:8294–8302. <https://doi.org/10.1002/2017GL074027>
- Brodsky EE, Mori JJ, Anderson L, Chester FM, Conin M, Dunham EM, Eguchi N, Fulton PM, Hino R, Hirose T, Ikari MJ, Ishikawa T, Jeppson T, Kano Y, Kirkpatrick J, Kodaira S, Lin W, Nakamura Y, Rabinowitz HS, Regalla C, Remitti F, Rowe C, Saffer DM, Saito S, Sample J, Sanada Y, Savage HM, Sun T, Toczko S, Ujije K, Wolfson-Schwehr M, Yang T (2020) The state of stress on the fault before, during, and after a major earthquake. *Annu Rev Earth Planet Sci* 48:49–74. <https://doi.org/10.1146/annurev-earth-053018-060507>

- Brown L, Wang K, Sun T (2015) Static stress drop in the M_w 9 Tohoku-oki earthquake: heterogeneous distribution and low average value. *Geophys Res Lett* 42:10595–10600. <https://doi.org/10.1002/2015GL066361>
- Byrne DE, Davis DM, Sykes LR (1988) Loci and maximum size of thrust earthquakes and the mechanics of the shallow region of subduction zones. *Tectonics* 7:833–857. <https://doi.org/10.1029/TC0071004p00833>
- Chester FM, Rowe C, Ujiie K, Kirkpatrick J, Regalla C, Remitti F, Moore, JC, Toy V, Wolfson-Schwehr M, Bose S, Kameda J, Mori JJ, Brodsky EE, Eguchi N, Tocco S, Expedition 343 and 343T Scientists (2013) Structure and composition of the plate-boundary slip zone for the 2011 Tohoku-Oki earthquake. *Science* 342:1208–1211. <https://doi.org/10.1126/science.1243719>
- DeMets C, Gordon RG, Argus DF (2010) Geologically current plate motions. *Geophys J Int* 181:1–80. <https://doi.org/10.1111/j.1365-246X.2009.04491.x>
- Di Toro G, Han R, Hirose T, De Paola N, Nielsen S, Mizoguchi K, Ferri F, Cocco M, Shimamoto T (2011) Fault lubrication during earthquakes. *Nature* 471:494–499. <https://doi.org/10.1038/nature09838>
- Du Y, Ma S, Kubota T, Saito T (2021) Impulsive tsunami and large runup along the Sanriku coast of Japan produced by an inelastic wedge deformation model. *J Geophys Res Solid Earth* 126:e2021JB022098. <https://doi.org/10.1029/2021JB022098>
- Fujiwara T, Kodaira S, No T, Kaiho Y, Takahashi N, Kaneda Y (2011) The 2011 Tohoku-Oki earthquake: displacement reaching the trench axis. *Science* 334:1240. <https://doi.org/10.1126/science.1211554>
- Fukahata Y, Wright TJ (2008) A non-linear geodetic data inversion using ABIC for slip distribution on a fault with an unknown dip angle. *Geophys J Int* 173:353–364. <https://doi.org/10.1111/j.1365-246X.2007.03713.x>
- Fukahata Y, Yagi Y, Mitui Y (2012) Absolute strain release in the 2011 Tohoku-oki Earthquake: waveform inversion and dynamic fault weakening. *J Geol Soc Japan* 118:396–409 (in Japanese with English abstract). <https://doi.org/10.5575/geosoc.2012.0040>
- Fukuyama E, Hok S (2015) Dynamic overshoot near trench caused by large asperity break at depth. *Pure Appl Geophys* 172:2157–2165. <https://doi.org/10.1007/s00024-013-0745-z>
- Fulton P, Brodsky E, Kano Y, Mori J, Chester F, Ishikawa T, Harris R, Lin W, Eguchi N, Toczko S (2013) Low coseismic friction on the Tohoku-Oki fault determined from temperature measurements. *Science* 342:1214–1217. <https://doi.org/10.1126/science.1243641>
- Hashimoto C, Noda A, Sagiya T, Matsu'ura M (2009) Interplate seismogenic zones along the Kuril-Japan trench inferred from GPS data inversion. *Nat Geosci* 2:141–144. <https://doi.org/10.1038/NNGEO421>
- Herman MW, Govers R (2020) Locating fully locked asperities along the South America subduction megathrust: a new physical interseismic inversion approach in a Bayesian framework. *Geochem Geophys Geosyst* 21:e2020GC009063. <https://doi.org/10.1029/2020GC009063>
- Herman MW, Furlong KP, Govers R (2018) The accumulation of slip deficit in subduction zones in the absence of mechanical coupling: implications for the behavior of megathrust earthquakes. *J Geophys Res Solid Earth* 123:8260–8278. <https://doi.org/10.1029/2018JB016336>
- Hirono T, Tsuda K, Kaneki S (2019) Role of weak materials in earthquake rupture dynamics. *Sci Rep* 9:6604. <https://doi.org/10.1038/s41598-019-43118-5>
- Hondori EJ, Park JO (2022) Connection between high pore-fluid pressure and frictional instability at tsunamigenic plate boundary fault of 2011 Tohoku-Oki earthquake. *Sci Rep* 12:12556. <https://doi.org/10.1038/s41598-022-16578-5>
- Hu Y, Wang K (2008) Coseismic strengthening of the shallow portion of the subduction fault and its effects on wedge taper. *J Geophys Res* 113:B12411. <https://doi.org/10.1029/2008JB005724>
- Ide S, Baltay A, Beroza GC (2011) Shallow dynamic overshoot and energetic deep rupture in the 2011 M_w 9.0 Tohoku-Oki earthquake. *Science* 332:1426–1429. <https://doi.org/10.1126/science.1207020>
- Iinuma T, Hino R, Kido M, Inazu D, Osada Y, Ito Y, Ohzono M, Tsushima H, Suzuki S, Fujimoto H, Miura S (2012) Coseismic slip distribution of the 2011 off the Pacific Coast of Tohoku Earthquake (M9.0) refined by means of seafloor geodetic data. *J Geophys Res* 117:B07409. <https://doi.org/10.1029/2012JB009186>
- Iinuma T, Hino R, Uchida N, Nakamura W, Kido M, Osada Y, Miura S (2016) Seafloor observations indicate spatial separation of coseismic and postseismic slips in the 2011 Tohoku earthquake. *Nat Commun* 7:13506. <https://doi.org/10.1038/ncomms13506>
- Iwasaki T, Sato H, Shinohara M, Ishiyama T, Hashima A (2015) Fundamental structure model of island arcs and subducted plates in and around Japan. Abstract T31B-2878 presented at the AGU Fall Meeting 2015, San Francisco, CA.
- Japan Agency for Marine-Earth Science and Technology [JAMSTEC] (2004) JAMSTEC seismic survey database. <https://doi.org/10.17596/0002069>
- Kajiura K (1963) The leading wave of a tsunami. *Bull Earthq Res Inst* 41:535–571. <https://doi.org/10.15083/000033711>
- Kido M, Osada Y, Fujimoto H, Hino R, Ito Y (2011) Trench-normal variation in observed seafloor displacements associated with the 2011 Tohoku-Oki earthquake. *Geophys Res Lett* 38:L24303. <https://doi.org/10.1029/2011GL050057>
- Kodaira S, No T, Nakamura Y, Fujiwara T, Kaiho Y, Miura S, Takahashi N, Kaneda Y, Taira A (2012) Coseismic fault rupture at the trench axis during the 2011 Tohoku-oki earthquake. *Nat Geosci* 5:646–650. <https://doi.org/10.1038/ngeo1547>
- Kodaira S, Fujiwara T, Fujie G, Nakamura Y, Kanamatsu T (2020) Large coseismic slip to the trench during the 2011 Tohoku-Oki earthquake. *Annu Rev Earth Plane Sci* 48:321–343. <https://doi.org/10.1146/annurev-earth-071719-055216>
- Koketsu K, Miyake H, Suzuki H (2012) Japan integrated velocity structure model version 1. In: Proceedings of the 15th world conference on earthquake engineering. https://www.iitk.ac.in/nicee/wcee/article/WCEE2012_1773.pdf
- Kostrov VV (1974) Seismic moment and energy of earthquakes, and seismic flow of rock. *Izv Earth Phys* 1:23–40
- Kubota T, Hino R, Inazu D, Ito Y, Iinuma T, Ohta Y, Suzuki S, Suzuki K (2017) Coseismic slip model of offshore moderate interplate earthquakes on March 9, 2011 in Tohoku using tsunami waveforms. *Earth Planet Sci Lett* 458:241–251. <https://doi.org/10.1016/j.epsl.2016.10.047>
- Kubota T, Saito T, Ito Y, Kaneko Y, Wallace LM, Suzuki S, Hino R, Henrys S (2018) Using tsunami waves reflected at the coast to improve offshore earthquake source parameters: application to the 2016 Mw 7.1 Te Araroa earthquake, New Zealand. *J Geophys Res Solid Earth* 123:8767–8779. <https://doi.org/10.1029/2018JB015832>
- Kubota T, Saito T, Tsushima H, Hino R, Ohta Y, Suzuki S, Inazu D (2021) Extracting near-field seismograms from ocean-bottom pressure gauge inside the focal area: application to the 2011 Mw 9.1 Tohoku-Oki earthquake. *Geophys Res Lett* 48:e2020GL091664. <https://doi.org/10.1029/2020GL091664>
- Lawson CL, Hanson BJ (1995) Solving least squares problems. *Soc Ind Appl Math Phila Pennsylvania*. <https://doi.org/10.1137/1.9781611971217>
- Lay T (2018) A review of the rupture characteristics of the 2011 Tohoku-oki Mw 9.1 earthquake. *Tectonophysics* 733:4–36. <https://doi.org/10.1016/j.tecto.2017.09.022>
- Lay T, Kanamori H, Ammon CJ, Koper KD, Hutko AR, Ye L, Yue H, Rushing TM (2012) Depth-varying rupture properties of subduction zone megathrust faults. *J Geophys Res* 117:B04311. <https://doi.org/10.1029/2011JB009133>
- Lin W, Conin M, Moore JC, Chester FM, Nakamura Y, Mori JJ, Anderson L, Brodsky EE, Eguchi N, Expedition 343 Scientists (2013) Stress state in the largest displacement area of the 2011 Tohoku-Oki earthquake. *Science* 339:687–690. <https://doi.org/10.1126/science.1229379>
- Lindsey EO, Mallick R, Hubbard JA, Bradley KE, Almeida RV, Moore JDP, Bürgmann R, Hill EM (2021) Slip rate deficit and earthquake potential on shallow megathrusts. *Nat Geosci* 14:321–326. <https://doi.org/10.1038/s41561-021-00736-x>
- Loveless JP, Meade BJ (2010) Geodetic imaging of plate motions, slip rates, and partitioning of deformation in Japan. *J Geophys Res* 115:B02410. <https://doi.org/10.1029/2008JB006248>
- Loveless JP, Meade BJ (2011) Spatial correlation of interseismic coupling and coseismic rupture extent of the 2011 M_w = 9.0 Tohoku-oki earthquake. *Geophys Res Lett* 38:L17306. <https://doi.org/10.1029/2011GL048561>
- Loveless JP, Meade BJ (2015) Kinematic barrier constraints on the magnitudes of additional great earthquakes off the east coast of Japan. *Seismol Res Lett* 86:202–209. <https://doi.org/10.1785/0220140083>
- Ma S (2012) A self-consistent mechanism for slow dynamic deformation and large tsunami generation for earthquakes in the shallow subduction zone. *Geophys Res Lett* 39:L11310. <https://doi.org/10.1029/2012GL051854>

- Ma S, Nie S (2019) Dynamic wedge failure and along-arc variations of tsunami genesis in the Japan Trench margin. *Geophys Res Lett* 46:8782–8790. <https://doi.org/10.1029/2019GL083148>
- Maeda T, Furumura T, Sakai S, Shinohara M (2011) Significant tsunami observed at ocean-bottom pressure gauges during the 2011 off the Pacific coast of Tohoku Earthquake. *Earth Planets Space* 63:803–808. <https://doi.org/10.5047/eps.2011.06.005>
- Maeda T, Takemura S, Furumura T (2017) OpenSWPC: An open-source integrated parallel simulation code for modeling seismic wave propagation in 3D heterogeneous viscoelastic media. *Earth Planets Space* 69:102. <https://doi.org/10.1186/s40623-017-0687-2>
- Maerten F, Resor P, Pollard D, Maerten L (2005) Inverting for slip on three-dimensional fault surfaces using angular dislocations. *Bull Seismol Soc Am* 95:1654–1665. <https://doi.org/10.1785/0120030181>
- Matsumoto K, Takanezawa T, Ooe M (2000) Ocean tide models developed by assimilating TOPEX/POSEIDON altimeter data into hydrodynamical model: a global model and a regional model around Japan. *J Oceanogr* 56:567–581. <https://doi.org/10.1023/A:1011157212596>
- Meade BJ (2007) Algorithms for the calculation of exact displacements, strains, and stresses for triangular dislocation elements in a uniform elastic half space. *Comput Geosci* 33:1064–1075. <https://doi.org/10.1016/j.cageo.2006.12.003>
- Miura S, Takahashi N, Nakanishi A, Tsuru T, Kodaira S, Kaneda Y (2005) Structural characteristics off Miyagi forearc region, the Japan Trench seismogenic zone, deduced from a wide-angle reflection and refraction study. *Tectonophysics* 407:165–188. <https://doi.org/10.1016/j.tecto.2005.08.001>
- Nakajima J, Hasegawa A (2006) Anomalous low-velocity zone and linear alignment of seismicity along it in the subducted Pacific slab beneath Kanto, Japan: reactivation of subducted fracture zone? *Geophys Res Lett* 33:L16309. <https://doi.org/10.1029/2006GL026773>
- Nishikawa T, Matsuzawa T, Ohta K, Uchida N, Nishimura T, Ide S (2019) The slow earthquake spectrum in the Japan Trench illuminated by the S-net seafloor observatories. *Science* 365:808–813. <https://doi.org/10.1126/science.aax5618>
- Noda H, Lapusta N (2013) Stable creeping fault segments can become destructive as a result of dynamic weakening. *Nature* 493:518–521. <https://doi.org/10.1038/nature11703>
- Noda A, Saito T, Fukuyama E (2018) Slip-deficit rate distribution along the Nankai Trough, southwest Japan, with elastic lithosphere and viscoelastic asthenosphere. *J Geophys Res Solid Earth* 123:8125–8142. <https://doi.org/10.1029/2018JB015515>
- Noda A, Saito T, Fukuyama E, Urata Y (2021) Energy-based scenarios for great thrust-type earthquakes in the Nankai trough subduction zone, southwest Japan, using an interseismic slip-deficit model. *J Geophys Res Solid Earth* 126:e2020JB020417. <https://doi.org/10.1029/2020JB020417>
- Remitti F, Smith SAF, Mittempergher S, Gualtieri AF, Di Toro G (2015) Frictional properties of fault zone gouges from the J-FAST drilling project (M_w 9.0 2011 Tohoku-Oki earthquake). *Geophys Res Lett* 42:2691–2699. <https://doi.org/10.1002/2015GL063507>
- Saito T (2019) *Tsunami generation and propagation*. Springer Japan, Tokyo. <https://doi.org/10.1007/978-4-431-56850-6>
- Saito T, Noda A (2022) Mechanically coupled areas on the plate interface in the Nankai trough, Japan and a possible seismic and aseismic rupture scenario for megathrust earthquakes. *J Geophys Res Solid Earth* 127:e2022JB023992. <https://doi.org/10.1029/2022JB023992>
- Satake K, Fujii Y, Harada T, Namegaya Y (2013) Time and space distribution of coseismic slip of the 2011 Tohoku earthquake as inferred from tsunami waveform data. *Bull Seismol Soc Am* 103:1473–1492. <https://doi.org/10.1785/0120120122>
- Sato M, Ishikawa T, Ujihara N, Yoshida S, Fujita M, Mochizuki M, Asada A (2011) Displacement above the hypocenter of the 2011 Tohoku-Oki earthquake. *Science* 332:1395. <https://doi.org/10.1126/science.1207401>
- Scholtz CH (1998) Earthquakes and friction laws. *Nature* 391:37–42. <https://doi.org/10.1038/34097>
- Shibazaki B, Noda H, Ikari MJ (2019) Quasi-dynamic 3D modeling of the generation and afterslip of a Tohoku-oki earthquake considering thermal pressurization and frictional properties of the shallow plate boundary. *Pure Appl Geophys* 176:3951–3973. <https://doi.org/10.1007/s00024-018-02089-w>
- Sun T, Wang K, Fujiwara T, Kodaira S, He J (2017) Large fault slip peaking at trench in the 2011 Tohoku-oki earthquake. *Nat Commun* 8:14044. <https://doi.org/10.1038/ncomms14044>
- Suwa Y, Miura S, Hasegawa A, Sato T, Tachibana K (2006) Interplate coupling beneath NE Japan inferred from three-dimensional displacement field. *J Geophys Res* 111:B04402. <https://doi.org/10.1029/2004JB003203>
- Suzuki K, Hino R, Ito Y, Yamamoto Y, Suzuki S, Fujimoto H, Shinohara M, Abe M, Kawaharada Y, Hasegawa Y, Kaneda Y (2012) Seismicity near the hypocenter of the 2011 off the Pacific coast of Tohoku earthquake deduced by using ocean bottom seismographic data. *Earth Planets Space* 64:1125–1135. <https://doi.org/10.5047/eps.2012.04.010>
- Tanioka Y, Satake K (1996) Tsunami generation by horizontal displacement of ocean bottom. *Geophys Res Lett* 23:861–864. <https://doi.org/10.1029/96GL00736>
- Tsushima H, Hino R, Tanioka Y, Imamura F, Fujimoto H (2012) Tsunami wave-form inversion incorporating permanent seafloor deformation and its application to tsunami forecasting. *J Geophys Res* 117:B03311. <https://doi.org/10.1029/2011JB008877>
- Uchida N, Bürgmann R (2021) A decade of lessons learned from the 2011 Tohoku-Oki earthquake. *Rev Geophys* 59:e2020RG000713. <https://doi.org/10.1029/2020RG000713>
- Ujije K, Tanaka H, Saito T, Tsutsumi A, Mori J, Toczko S (2013) Low coseismic shear stress on the Tohoku-Oki megathrust determined from laboratory experiments. *Science* 342:1211–1214. <https://doi.org/10.1126/science.1243485>
- Wang K, Dixon T (2004) “Coupling” semantics and science in earthquake research. *Eos Trans Am Geophys Union* 85:180. <https://doi.org/10.1029/2004EO180005>
- Wang K, Sun T, Brown L, Hino R, Tomita F, Kido M, Iinuma T, Kodaira S, Fujiwara T (2018) Learning from crustal deformation associated with the M9 2011 Tohoku-oki earthquake. *Geosphere* 14:2. <https://doi.org/10.1130/GES01531.1>
- Watanabe S, Ishikawa T, Nakamura Y, Yokota Y (2021) Co- and postseismic slip behaviors extracted from decadal seafloor geodesy after the 2011 Tohoku-oki earthquake. *Earth Planets Space* 73:162. <https://doi.org/10.1186/s40623-021-01487-0>
- Wessel P, Luis JF, Uieda L, Scharroo R, Wobbe F, Smith WHF, Tian D (2019) The generic mapping tools version 6. *Geochem Geophys Geosys* 20:5556–5564. <https://doi.org/10.1029/2019GC008515>
- Yabuki T, Matsu'ura M (1992) Geodetic data inversion using a Bayesian information criterion for spatial distribution of fault slip. *Geophys J Int* 109:363–375. <https://doi.org/10.1111/j.1365-246X.1992.tb00102.x>
- Yagi Y, Fukahata Y (2011) Rupture process of the 2011 Tohoku-oki earthquake and absolute elastic strain release. *Geophys Res Lett* 38:L19307. <https://doi.org/10.1029/2011GL048701>
- Yamazaki Y, Cheung KF, Lay T (2018) A self-consistent fault slip model for the 2011 Tohoku earthquake and tsunami. *J Geophys Res Solid Earth* 123:1435–1458. <https://doi.org/10.1002/2017JB014749>

Publisher's Note

Springer Nature remains neutral with regard to jurisdictional claims in published maps and institutional affiliations.